

Dated: 6 August 2021

The Virgo Collaboration + additional authors

. To be submitted to CQG

Virgo INTERNAL DOCUMENT – NOT FOR PUBLIC DISTRIBUTION

The Virgo O3 run and the impact of the environment

The Virgo Collaboration + T. Avgitas and J. Marteau from IP2I Lyon (if not in the author list yet) + C. Giunchi and M. Oliveri from INGV + M. Coughlin from University of Minnesota + N Mukund from Albert-Einstein-Institut, Max-Planck-Institut für Gravitationsphysik, Hannover + E. Caredda (EGO intern from UBologna)...

Abstract. Sources of geophysical noise (such as wind, sea waves and earthquakes) or of anthropogenic noise impact ground-based gravitational-wave interferometric detectors, causing transient sensitivity worsening and gaps in data taking. During the one year-long third Observing Run (O3: from April 01, 2019 to March 27, 2020), the Virgo Collaboration collected a statistically significant dataset, used in this article to study the response of the detector to a variety of environmental conditions. We correlated environmental parameters to global detector performance, such as observation range, duty cycle and control losses. Where possible, we identified weaknesses in the detector that will be used to elaborate strategies in order to improve Virgo robustness against external disturbances for the next data taking period, O4, currently planned to start in the second semester of 2022. The lessons learned could provide useful insights as well for the design of the next generation of ground-based interferometers.

23	Contents	
24	1 Introduction	3
25	2 The Virgo environmental monitoring during O3	5
26	3 Seismic noises	7
27	3.1 The seismic frequency bands and their evolution during the O3 run . . .	7
28	3.2 Impact on the Virgo detector	11
29	3.2.1 Sensitivity	11
30	3.2.2 Duty cycle	11
31	4 Earthquakes	13
32	4.1 Seismon and O3 setup at EGO	14
33	4.2 Earthquakes impact during O3	15
34	4.3 Plans for O4	20
35	5 Bad weather	22
36	5.1 Impact of sea activity	22
37	5.1.1 Microseism impact on strain noise	22
38	5.1.2 Microseism impact on glitch rates	23
39	5.1.3 Microseism and scattered light	24
40	5.1.4 Identification of scattered light culprits	26
41	5.2 Impact of wind	28
42	5.3 Disentangling sea activity and wind	29
43	6 Other environment impacts	31
44	6.1 Magnetic noise	31
45	6.2 Lightnings	32
46	6.3 Cosmic muons	34
47	7 Outlook and prospects for O4	35
48	Appendix A the lock losses during O3	37

49 1. Introduction

50 The past decade has seen the ramp-up of the second-generation ('Advanced') earth-based
51 gravitational-wave (GW) detectors. Design improvements and technological upgrades
52 have paved the way to the first direct detections of GWs by the global network made up
53 of the two aLIGO instruments [1] (located in the USA: Hanford, WA and Livingston,
54 LA) and of the Advanced Virgo detector [2] (located in Cascina, Italy). The main
55 results achieved by the LIGO Scientific Collaboration and the Virgo Collaboration –
56 recently joined by the KAGRA collaboration whose detector [3], located under the
57 Kamioka mountain in Japan, is nearing completion – include the first detection of
58 a binary black hole merger (GW150914 [4]); the first detection of a binary neutron
59 star merger (GW170817 [5]) that lead to the birth of multi-messenger astronomy with
60 GW [6]; and now dozens of detections of compact binary mergers that add up in a GW
61 Transient Catalogue regularly updated [7, 8]. These detections contribute to opening
62 a new window onto the Universe by providing insights to the populations of compact
63 objects and the binary merger rates [9]; they also allow scientists to perform stringent
64 tests of general relativity [10] in a new regime of gravitation never probed before.

65 The operation of ground-based GW detectors is organized into successive steps forming a
66 recurring sequence over the years: upgrades; commissioning and sensitivity improvement
67 (the so-called *noise hunting* phase); data-taking periods called observing runs (or simply
68 runs and labelled *On*). So far there have been three runs for the global network of
69 advanced detectors.

- 70 • O1 (09/2015 – 01/2016) with only the two LIGO detectors taking data;
- 71 • O2 (11/2016 – 08/2017) with Virgo joining LIGO on August 01;
- 72 • finally O3 (04/2019 – 03/2020), that saw the three detectors take data jointly
73 during 11 months in total: 6 months first (called O3a), followed by a 1-month
74 break (October 2019) and then another period of 5 months of data taking (O3b),
75 interrupted about a month earlier than expected due to the worldwide COVID-19
76 pandemic.

77 The above listing shows that the O3 run was the first long data-taking period for the
78 Advanced Virgo detector. Therefore, we have used the wealth of unprecedented data
79 collected during this year to make an in-depth analysis of the instrument performance.
80 In this article, we study the impact of the environment on Advanced Virgo, along the
81 lines of previous publications from Virgo [11], LIGO [12] or KAGRA [13]. We focus on
82 various types of seismic noises, on earthquakes and on bad weather periods. We also
83 briefly investigate the effect of other possible disturbances: magnetic noise, lightning
84 and cosmic muons. Our goal is threefold: to quantify how the Virgo sensitivity and
85 duty cycle depend on these external parameters; to use this knowledge to prepare the
86 next run, O4, scheduled to start in the second semester 2022; finally, to build experience
87 for future GW detectors, in particular the Einstein Telescope project [14].

88 The Virgo detector is located in Italy at EGO, the European Gravitational Observatory,
89 in the municipality of Cascina. The EGO site is in the countryside, about 12 km south-
90 east of Pisa and about 17 km east of the Tyrrhenian coast. Virgo is not far from some
91 industrial and commercial sites that can generate noise. Within 7 km from EGO there
92 are: elevated highways, railway tracks, wind turbines, earth quarries, electroducts and
93 the Pisa airport. To avoid pressure waves potentially shaking the ground, no-fly zones
94 have been enforced in cylindrical volumes (600 m radius and height) above the Virgo
95 experimental buildings.

96 Advanced Virgo is a power-recycled Michelson interferometer with Fabry-Perot cavities
97 in its 3 km-long arms. All core optics are suspended to long suspensions, called the
98 superattenuators [15], that have a twofold use: first, to isolate as much as possible the
99 mirrors from seismic motions (both vertical and longitudinal), and then to control very
100 accurately their positions in all six degrees of freedom. Many feedback systems are
101 used to bring the detector to its working point and maintain it there [16, 17]. This
102 configuration – the same for O2 and O3: the Michelson interferometer on a dark fringe,
103 the Fabry-Perot and power recycling cavities in resonance – is the only one in which the
104 detector is sensitive to the passing of GWs.

105 The phase leading to the acquisition of the Virgo working point is called *locking*. The
106 detector is said to be *locked* when it is kept at its working point by its global control
107 system. A *lock loss* is a moment when the detector cannot be controlled anymore and
108 its working point is lost. The most common sequence during data taking is locking →
109 locked → data taking in Science mode → lock loss → locking again, etc.

110 During a run, priority is obviously given to taking data of quality good enough to be
111 included in physics analysis. In Virgo, this mode is called *Science*. During O3, the
112 average duty cycle in Science mode has been around 76% [18], with the remaining time
113 divided almost equally into three categories.

- 114 • Locking and adjustment phases, to restore the Science working point and restart
115 taking data;
- 116 • Recurring controlled actions on the detector: maintenance (usually a few hours
117 on Tuesday mornings local time), calibration (usually every Wednesday evening)
118 or commissioning (measurements, working point tuning or tailored improvements:
119 sessions organized when the need arises);
- 120 • Problems preventing a smooth running of the detector.

121 The article is organized as follows. Section 2 describes the environmental monitoring
122 of the Virgo detector during the O3 run. Section 3 is dedicated to the different seismic
123 noise contributions (either natural or human-related): how to disentangle them, how
124 to monitor them and what their impacts on the detector are in terms of sensitivity
125 and duty cycle. Section 4 provides an analysis of the impact of earthquakes on the
126 detector: earthquakes both strong and distant (for which the arrival of potentially

127 strong seismic waves can be anticipated), such as weak but much closer ones, have
 128 been found to cause lock losses, thus reducing the Virgo duty cycle. Section 5 studies
 129 the impact of bad weather on data quality and duty cycle, disentangling contributions
 130 from the sea activity and the wind. Section 6 goes through other environment impacts:
 131 magnetic noise, lightning and a study of the cosmic muon rate on the Virgo central
 132 building. Then, Section 7 concludes this article by opening outlooks to the future O4
 133 run. Finally, Appendix A provides a detailed and quite complete classification of the
 134 lock losses during the O3 run. Although that study has a scope broader than the
 135 present article, it is included here for reference and also because its results were used,
 136 in particular to find out which control losses were due to earthquakes.

137 **2. The Virgo environmental monitoring during O3**

138 The Virgo detector is equipped with a large set of probes used to monitor the conditions
 139 of the nearby environment. Since these conditions can influence the detector response, or
 140 even mimic a GW event, it is very important to track their evolution to assess the right
 141 working condition of the detector or to use them as veto against possible interference.

142 The set of probes and their conditioning electronics constitute the Environmental
 143 Monitoring System (EMS). The EMS was initially composed by a few tens of probes [19]
 144 and then improved during the detector upgrades that occurred in the past years. During
 145 O3, the total number of channels belonging to EMS was about 420.

146 The EMS is also helpful to understand the origin of some noise sources affecting
 147 the detector sensitivity. Indeed it was largely used during the commissioning phases
 148 following the detector upgrades, to recover and improve the Virgo performances in
 149 terms of sensitivity and duty cycle [11].

150 Two kinds of probes are available in EMS: the first one are slow monitoring probes
 151 for temperature, pressure, humidity, weather and lightning monitoring, all recorded at
 152 1 Hz sampling rate. The second kind are fast probes like seismometers, accelerometers,
 153 episensors[‡], magnetometers, microphones, voltage and current sensors, radio-frequency
 154 (RF) antennas, recorded up to 20 kHz sampling rate.

155 The main characteristics: type, model and frequency band of the environmental probes
 156 in use during O3 are listed in Table 1. Figure 1 shows the arrangement of the
 157 environmental monitoring probes inside the main Virgo buildings. Most probes are
 158 located in the experimental halls of the relevant buildings of the detector: Central
 159 Building (CEB), North and West End Buildings (NEB and WEB) and Mode Cleaner
 160 Building (MCB). Usually, the probes are placed on the critical elements of the detector,
 161 like the walls of the vacuum chambers containing the test mass suspensions, or the
 162 optical benches hosting the laser injection and GW detection systems.

[‡] Episensors are triaxial, strong motion accelerometers.

Type	Model	Frequency Band
Seismometer	Guralp CMG-40T	0.01 – 50 Hz
Episensor	Kinometrics FBA ES-T	0.1 – 200 Hz
Accelerometer	Wilcoxon 731-207 or PCB 393B12	1 – 1000 Hz
Magnetometer	Metronics MFS-06 or MFS-06e	0.1 mHz – 10 kHz
Microphone	Brüel & Kjær 4190 or 4193	0.1 – 10 kHz
RF antenna	AAS STA 5 A/D/0.01-100	10 kHz – 100 MHz
Voltage probe	Talema 0015P1-2-009	DC – 10 kHz
Current probe	IME 0015P1-2-009	DC – 10 kHz
Temperature probe	Analog Device AD590	DC – 0.5 Hz
Humidity probe	Honeywell HIH-5031-001	DC – 0.5 Hz
Pressure probe	NXP MPXA4115A6U	DC – 0.5 Hz
Weather station	Davis Advantage Pro 2	DC – 0.3 Hz
Lightning detector	Boltek LD 250	DC – 0.5 Hz

Table 1: Characteristics of the Virgo environmental probes during O3.

163 Few probes are placed outside the buildings and are not shown in the schematics,
 164 namely the weather station, the lightning detector and two additional magnetometers.
 165 These two low-noise induction coil magnetometers are deployed at 0.5 m depth in the
 166 soil, at about 100 m from the CEB, oriented along the geographic North and West
 167 directions. Their data are shared in real time with the <http://www.vlf.it> EM antenna
 168 network [20].

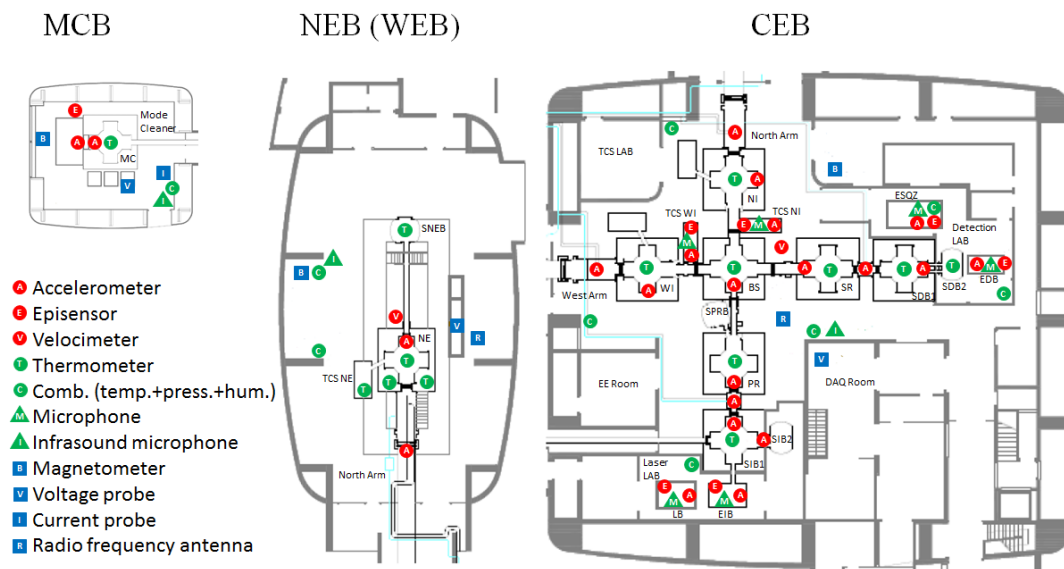


Figure 1: Location of the probes used for the Virgo environmental monitoring system. Maps of most relevant building are shown: left MCB, middle NEB, right CEB. The WEB is very similar to NEB and is not shown.

169 3. Seismic noises

170 In this section we introduce the main sources of seismic noise at the Virgo site. They are
171 disentangled and monitored by examining seismic probes in specific frequency bands.
172 We provide a statistical description of the noise and evidence its main recurring features.
173 Then, we describe how they impacted on the detector during the O3 run.

174 3.1. The seismic frequency bands and their evolution during the O3 run

175 The seismic wavefield at EGO, the site of the Virgo detector, is the sum of several
176 sources [21]. Seismic spectra variability during the O3 run is illustrated in Fig. 2. The
177 largest contribution to seismic ground motion in the frequency range between 0.1 Hz
178 and 1 Hz, referred to as *microseism*, is due to the interaction between sea waves and the
179 bottom of the sea [22, 23]. At EGO, the prevailing microseismic peak is around 0.35 Hz.
180 Figure 3 shows the time evolution of microseism during the O3 run, while Fig. 4 shows
181 the corresponding cumulative distribution, split by season. Microseism intensity follows
182 seasonal variations, being larger in fall and winter, due to the stronger wind and sea
183 activity.

184 Above 1 Hz, anthropogenic sources dominate. Heavy vehicles (trucks and alike) on
185 ~ 1 km distant elevated roads are the prevailing source of seismic noise in the 1-10 Hz
186 band [21]. As illustrated in Fig. 5, the RMS of seismic noise in the 1-5 Hz band follows
187 a working day/night cycle with higher levels during working hours (from 8:00 to 17:00
188 local time – LT), shallow deeps at lunch times (12:00-14:00 LT) and minima during
189 week-ends and holidays. For instance, the noise reduction during the two consecutive
190 Wednesdays, Christmas 2019 and the New Year’s Day 2020, is quite impressive. A
191 significant reduction is also visible during the Spring 2020 lockdown in Italy, due to the
192 COVID-19 pandemic.

193 Finally, above 10 Hz, the dominant seismic contribution is generated locally: vehicles in
194 nearby and on-site roads, agricultural work on neighbouring land, etc. Figure 6 shows
195 the average day-night variations, computed in the 10-40 Hz band on a weekly basis: in
196 blue during the O3 run; in magenta during the 1-month commissioning break (October
197 2019) separating the two halves of O3; finally in orange for the second semester of
198 2020, during which hardware upgrades and construction or infrastructure works for the
199 Advanced Virgo+ project [25] took place. The common feature between the three curves
200 is the dominant peak on Tuesday mornings, the usual slot for the weekly maintenance
201 of the Virgo detector. This activity includes in particular the refilling of Nitrogen §
202 tanks by heavy trucks coming on-site, and the possibility to have people moving around
203 and working inside experimental areas whose access is forbidden during data taking
204 periods. The on-site seismic noise level was slightly higher during the commissioning

§ Liquid Nitrogen is used to cool down the Advanced Virgo cryotrap [2].

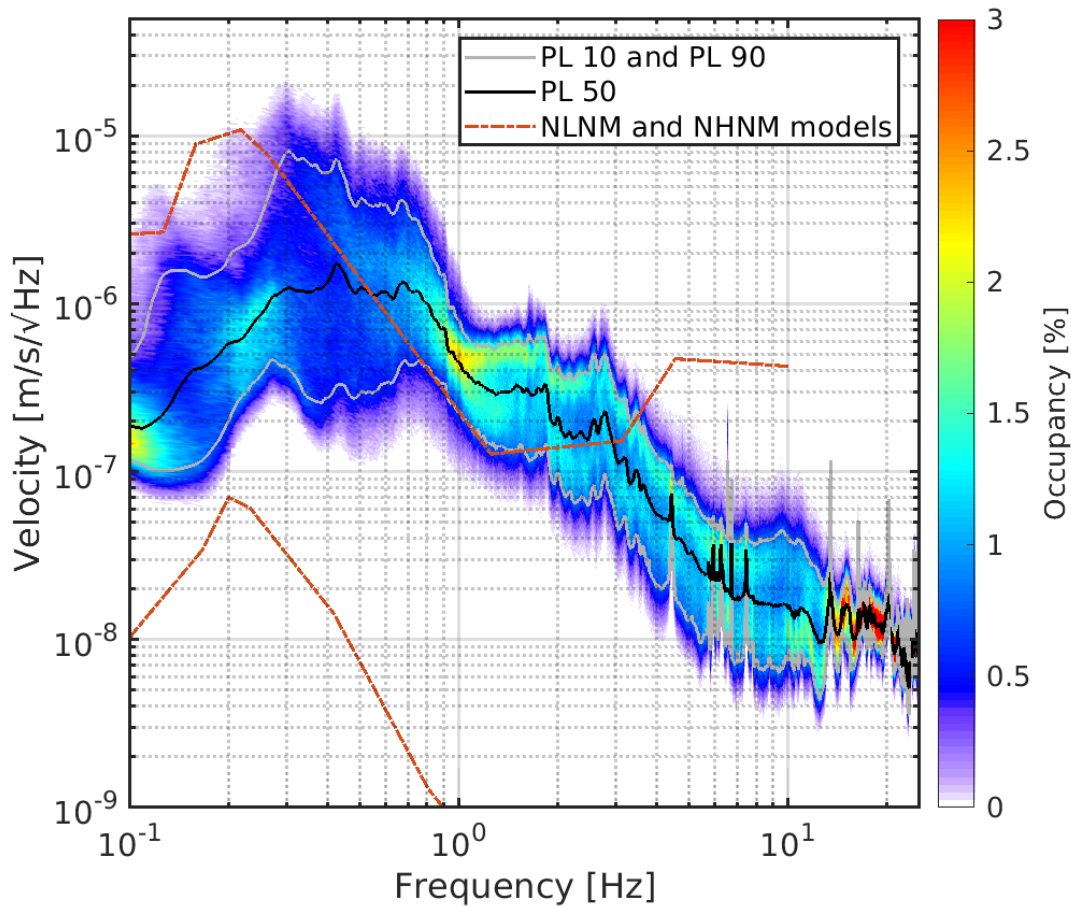


Figure 2: Variability of horizontal velocity of the Virgo NEB ground floor during O3. The quantity shown is the 2D histogram of velocity amplitude spectra computed every 128 seconds during all O3 science time. The color scale indicates the percent occupancy of histogram bins. The superposed continuous curves show different percentile levels (labelled *PL* on the plot): 10% (gray), 50% (black) and 90% (gray as well). The two red dashed curves correspond to the Peterson low-noise ('NLNM') and high-noise ('NHNM') models [24].

205 break compared to the O3 run, but not by much: that shutdown was not long enough
 206 to allow for invasive works that could have jeopardized the restart of data taking on
 207 November 01, 2019, alongside the two LIGO detectors. On the other hand, on-site
 208 activities are more evenly distributed over working days during the post-O3 upgrade.
 209 Though, activities were the lowest on weekends during that period because of site access
 210 restrictions, enforced because of the pandemic.

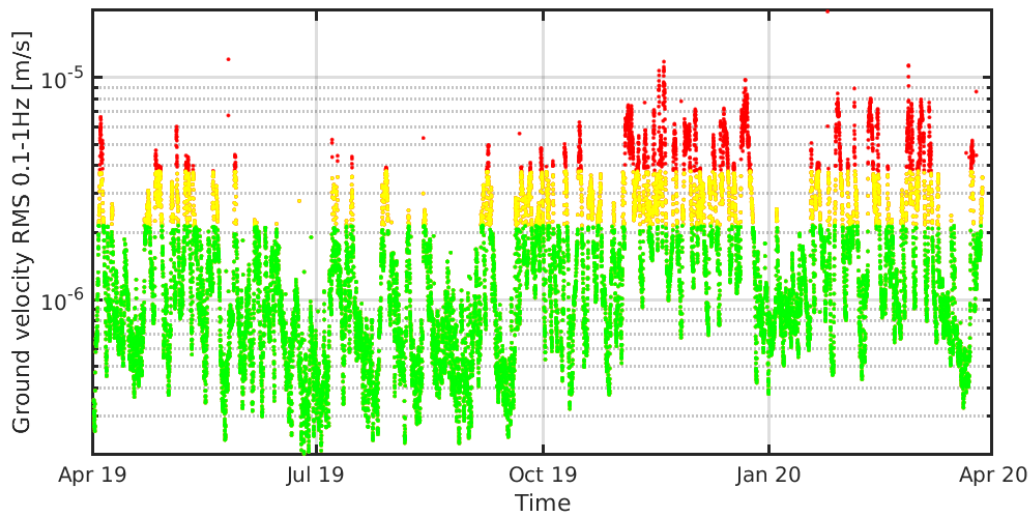


Figure 3: Evolution during O3 of seismic RMS in the 0.1 to 1 Hz frequency band. Data colored in yellow and red exceed the 75th and 90th percentile, respectively.

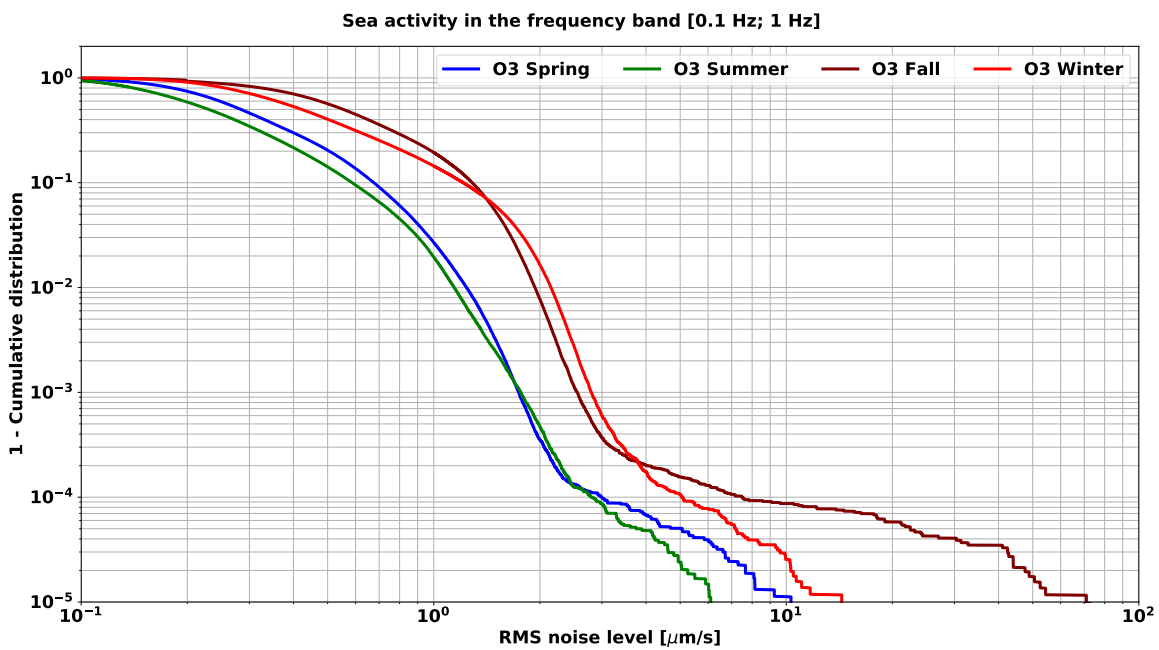


Figure 4: Cumulative distribution of the sea-induced seismic noise (frequency band: 0.1-1 Hz) measured at EGO during each season in 2019-2020.

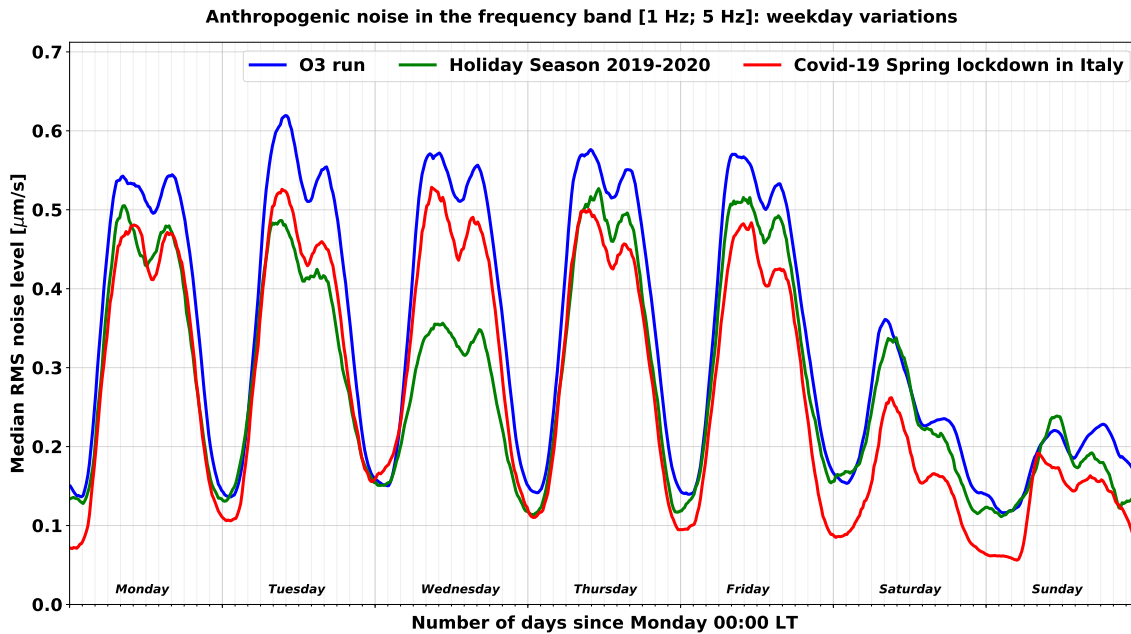


Figure 5: Average evolution on a weekly basis of the seismic anthropogenic noise (frequency band: 1-5 Hz) measured at EGO during different times in 2019-2020.

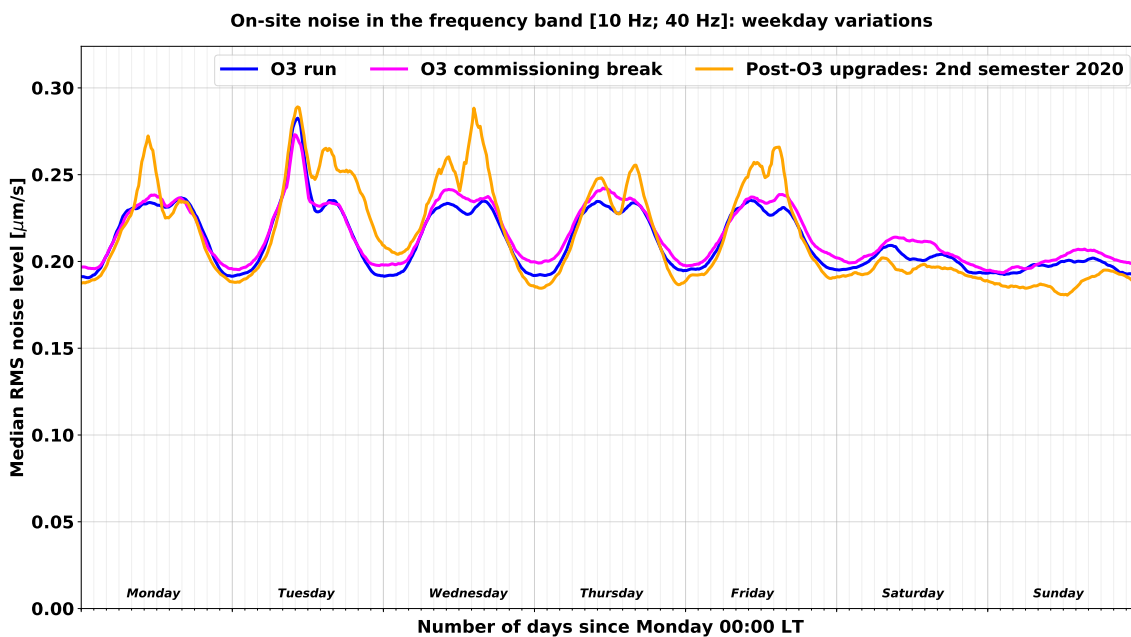


Figure 6: Average evolution on a weekly basis of the seismic on-site noise (frequency band: 10-40 Hz) measured at EGO during different times in 2019-2020.

211 *3.2. Impact on the Virgo detector*

212 The previous sections have demonstrated that the Virgo collaboration has deployed
 213 an accurate monitoring of the environment at EGO and that the recorded data show
 214 significant variations over time, in agreement with expectations from known noise
 215 sources. It is then interesting to see how these noises impact the performance of the
 216 Virgo detector, namely its sensitivity and duty cycle.

217 *3.2.1. Sensitivity* A convenient way to monitor the sensitivity of a gravitational-wave
 218 detector like Virgo is to study the evolution of the associated BNS range. That figure-
 219 of-merit provides the average distance up to which the merger of a standard binary
 220 neutron star system (BNS) can be detected with a signal-to-noise ratio (SNR) set to 8
 221 by convention. The average is taken over the position of the BNS in the sky and over
 222 the orientation of its orbital plane. Broadly speaking, the lower (higher) the noise in the
 223 frequency band of interest –from a few tens of Hz to a few hundreds of Hz depending
 224 on the actual sensitivity curve –, the larger (smaller) the BNS range.

225 In addition to its potential dependence on the environment, the BNS range can fluctuate
 226 significantly due to changes in the control accuracy of the detector. Therefore, averaging
 227 raw BNS range values, especially over long timescales, is not expected to provide
 228 meaningful information as one would mix together too many effects that cause the
 229 BNS range to vary. Therefore, the method used in the following consists in computing
 230 a moving daily average of the BNS range and to focus on the local fluctuations around
 231 this level. Figures 7 and 8 show these variations, averaged over the whole O3 run, and
 232 projected over a weekly or daily time range, respectively. On both plots, the red dots
 233 show daily variations while the blue curve is a moving median profile of the scatter plot.
 234 The variations seen are clearly of anthropogenic origin, with a day-night pattern and a
 235 reduced spread during the weekend. Although they are significant, they are also limited
 236 in size: ~ 1 Mpc compared to an average BNS range of about 50 Mpc during the O3
 237 run, hence a $\sim 2\%$ fluctuation. This shows the robustness of the Virgo detector.

238 *3.2.2. Duty cycle* Figure 9 shows the average duty cycle of the Virgo detector during
 239 the O3 run. The top plot displays its average variation over a week, while the bottom one
 240 focuses on a day. The red curve normalizes the Science mode data taking by the elapsed
 241 real time, while the green one is computed by excluding the calibration, commissioning
 242 and maintenance periods. Thus, the latter curve shows the fraction of the time available
 243 for data taking that is actually used for that. Activities on the detector are concentrated
 244 during working hours as expected, with maintenance on Tuesday morning, calibrations
 245 on Wednesday evenings and commissioning slots from Monday to Friday depending on
 246 the needs. There is a non-negligible recovery time from maintenance, while the transition
 247 from calibration back to data taking is smoother and quicker on average. During the

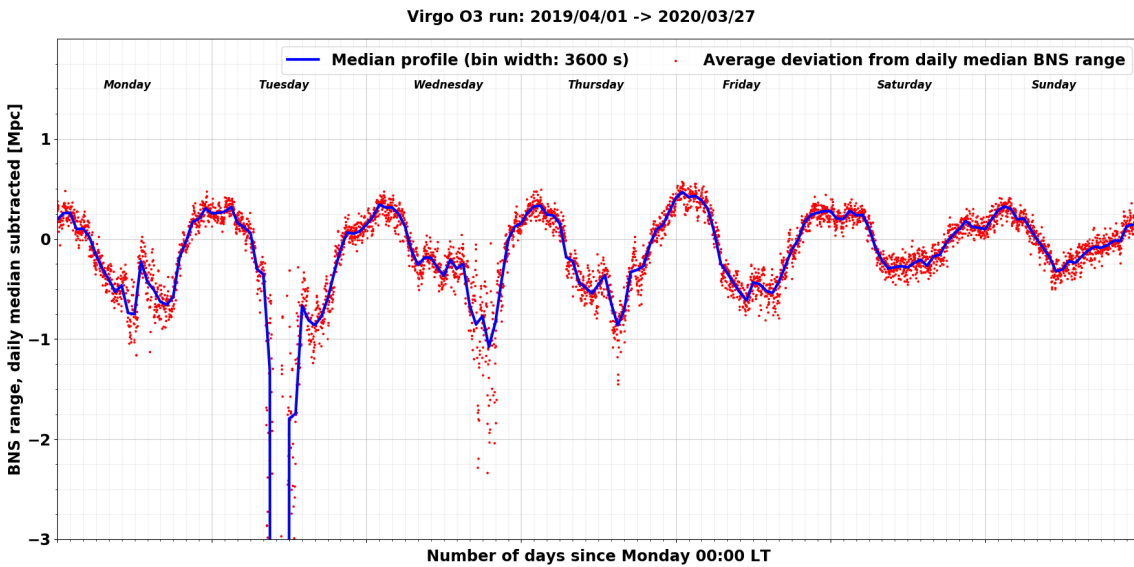


Figure 7: Average variation of the BNS range around its local average, computed on a weekly basis. The blue trace is a moving median profile of the red scatter plot, each dot showing the fluctuation at a particular weekday and time. The lack of available data on Tuesday morning corresponds to the weekly maintenance period of the Virgo detector, while the sharper variations on Wednesday and Thursday afternoons are due to the fact that these times have often been used for calibration or detector activities. Therefore, the BNS range is less stable than usually when nominal data taking gets restored.

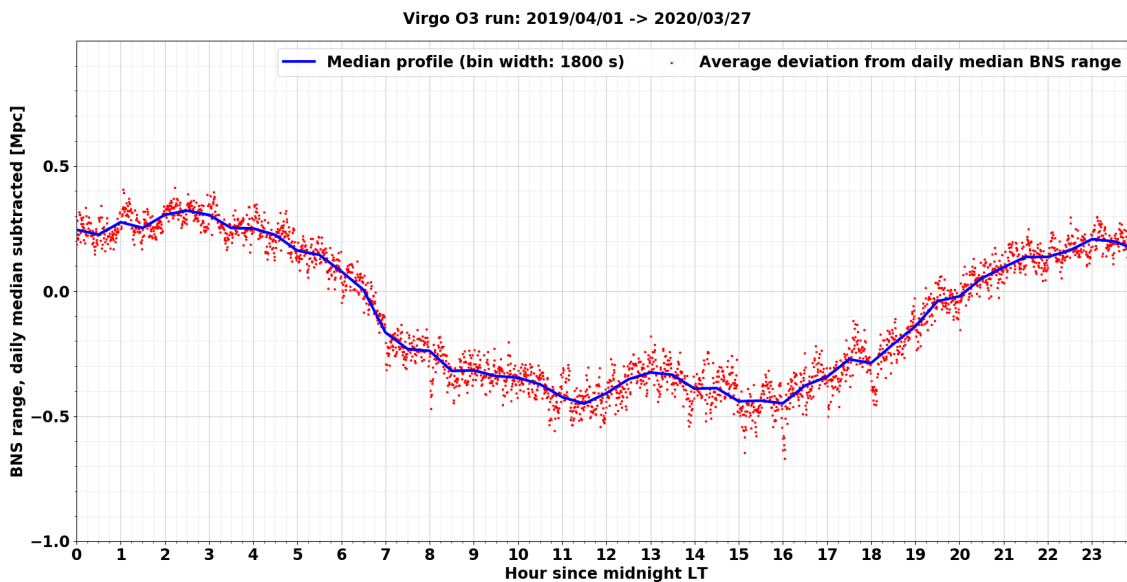


Figure 8: Average variation of the BNS range around its local average, computed on a daily basis. The blue trace is a moving median profile of the red scatter plot, each dot showing the fluctuation at a particular time of the day.

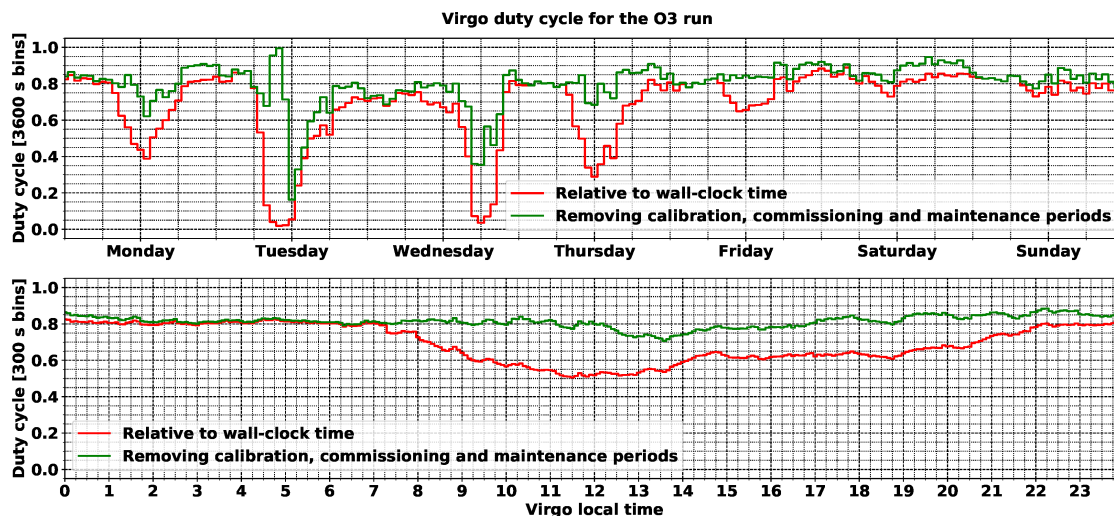


Figure 9: Average weekly (top) and daily (bottom) duty cycle of the Virgo detector during the O3 run. The red curve uses the elapsed real time as normalization, while the green one is produced excluding the times spent doing calibration, commissioning or maintenance, three activities that are incompatible with Science-mode data taking.

248 quietest hours of the night, when no work takes place on the interferometer except in
 249 case of an emergency, the average duty cycle reaches a plateau around 85%.

250 4. Earthquakes

251 Earthquakes produce different types of seismic waves. The body waves that travel
 252 through the Earth are usually detected first. The fastest are the primary waves ('P-
 253 waves') that are longitudinal compression waves. Their speed depends on the medium
 254 in which they propagate and can reach a maximum of 8 km/s. The secondary waves (S-
 255 waves) are transverse shear waves whose speed is about twice smaller. The surface waves
 256 (mostly of Rayleigh type) attenuate more slowly and are dominant at long distances from
 257 the earthquake source. For this reason, their amplitude far from the epicenter is greater
 258 than that of body waves. Rayleigh waves originate from P-wave and S-wave (with
 259 vertical polarization) coupling at the Earth surface. The result is a wave with both
 260 longitudinal and transversal components and a propagation speed up to a few km/s.
 261 Due to their transversal motion and slow attenuation, the surface waves are responsible
 262 for most of the damages caused by strong earthquakes.

263 Seismic waves strong enough at the EGO site can saturate the feedback systems that
 264 keep Virgo at its nominal working point where it is sensitive to the passing of GWs.
 265 Following each control loss (regardless of its origin: an earthquake or another cause),
 266 data taking stops immediately and can only restart after the completion of the semi-
 267 automated sequence that allows restoring the Virgo global working point – during the

268 O3 run, that procedure took about 20 minutes on average [18]. But the time lost can
269 be much longer in case of a control loss due to an earthquake, in case the suspensions
270 are excited by the seismic waves. In that case, one may have to wait up to one hour
271 after the event that the high-quality factor modes of the suspensions have cooled down,
272 before initiating the control acquisition procedure. Since each lock loss reduces the
273 Virgo duty cycle, it is therefore important to understand which fraction of these are due
274 to earthquakes, and what are the earthquakes that induce them.

275 One obvious category are strong earthquakes that occur along the boundaries of the
276 main tectonic plates. Most of them are quite distant from EGO, meaning that a low-
277 latency framework relying on data from a variety of seismic stations worldwide could
278 produce early warning notices that would be received and processed *ahead* of the seismic
279 waves. In that case, one could take preventive measures to try to mitigate the effect of
280 the ground shaking, with the goal to avoid the lock loss. In the following, we describe the
281 strategy implemented at Virgo during the O3 run and relying on a framework developed
282 at LIGO – an example of the existing teamwork among members of the global GW
283 detector network.

284 Furthermore, as explained below, the study has also highlighted another contribution
285 from much weaker earthquakes, quite close to EGO. Those have been more difficult to
286 identify as they do not lead to early warnings and the frequency of their seismic waves
287 is much higher when they arrive at EGO: up to ~ 1 Hz, whereas teleseism waves are in
288 the frequency band 10 – 100 mHz. In addition, the proximity of their epicenters makes
289 useless the use of warnings that would always come too late. Thus, the only way to
290 mitigate these earthquakes is to understand how they impact the Virgo control system
291 and what could be done to strengthen it.

292 *4.1. Seismon and O3 setup at EGO*

293 In addition to making the whole detector as robust as possible against the passing of
294 strong seismic waves, the only other leverage one can use to mitigate the impact of
295 earthquakes is to rely on early warnings provided by worldwide arrays of seismometers.

296 Following initial tests done during the O2 run and the upgrade period that followed, we
297 ran at EGO during O3 an instance of the Seismon [26, 27, 28] framework, developed
298 by LIGO to process earthquake early warnings provided by the US Geological Survey
299 (USGS) [29] and to compute information relevant for each site of the LIGO-Virgo
300 network. Namely, predictions for the arrival time of the different types of seismic waves,
301 for the maximal amplitude of the ground motion and a probability to lose the detector
302 control due to that earthquake. That framework was split into four consecutive steps,
303 each associated with a server integrated within the EGO online data acquisition system
304 (DAQ) system used to steer and monitor the Virgo detector.

- 305 • Reception of the USGS alerts.

- 306 • Processing of each alert by the Seismon framework.
- 307 • Extraction of the subset of Seismon data pertinent to the EGO site and provision
- 308 to the Virgo online framework.
- 309 • Local processing of these data.

310 In addition to producing a plot summarizing all information from the early warning,
311 a loose cut is applied on magnitude and distance to estimate whether the earthquake
312 could be relevant, meaning that it could impact the control of the Virgo detector.

313 In that case, and if the warning was quick enough to precede the arrival of the
314 seismic wave on-site, an alarm would latch on the main panel of the Virgo Detector
315 Monitoring System [30, 31], alerting the operator on duty in the control room.

316 In the nominal O3 control configuration, the two 3 km-long optical cavities are kept in
317 resonance by acting on the end mirror suspensions: their actuators are the least noisy,
318 at the price of a reduced correction range. Actuators located at the level of the input
319 mirror suspensions have higher dynamics but introduce slightly more noise as well. A
320 smooth transition procedure, working both ways without losing the detector control,
321 has been developed to allow switching from one configuration to the other, and back.
322 During the O3 run, the procedure in use was the following: once alerted by Seismon, the
323 operator on duty would monitor the optics suspension status and trigger the transition
324 nominal mode \rightarrow earthquake mode (EQ mode) manually when the test mass suspensions
325 would start shaking significantly. Once activated, that process would take a few tens of
326 seconds to complete. Then, either the detector would nevertheless lose its working point
327 (and the control acquisition procedure would have to be restarted from the beginning),
328 or the EQ mode control would be kept until the whole seismic wave trains has passed
329 by and the suspensions motion has been damped back to levels low enough to allow
330 resuming the nominal control mode.

331 Unrelated to earthquakes, the EQ mode was also found useful during periods of high
332 wind: gusts make the building structures (walls and floors) shake and those vibrations
333 can couple to the suspensions, potentially causing control corrections to saturate. During
334 most of O3, the EQ mode was used parsimoniously as its configuration had not been
335 validated for the production of good quality data for physics analysis. Therefore, setting
336 it could mean keeping the detector controlled for a longer time, but the data produced
337 would have had to be discarded. But, a few weeks before the end of the run, the EQ
338 mode got finally qualified for regular data taking and later studies [32] showed that there
339 was no significant degradation of the Virgo sensitivity when switching to it. Therefore,
340 it was used more regularly from that time; the possibility to have such a backup solution
341 for O4 as well will be studied in the coming months.

342 *4.2. Earthquakes impact during O3*

343 The stronger and/or the closer to EGO the earthquake, the more likely it is to impact
344 the control of the Virgo detector. To study the impact of strong regional earthquakes

345 or teleseisms, the USGS warnings processed by Seismon are sufficient. But it was soon
 346 realized that some close earthquakes – from a few tens to a few hundreds kilometers
 347 away from EGO –, too weak to appear on the list of USGS alerts processed by Seismon,
 348 could have caused losses of the control of Virgo. Therefore, to also investigate these
 349 other cases, a query [33] was made to the public INGV earthquake website [34], in
 350 order to download all earthquakes recorded during O3 in the Mediterranean area. This
 351 list of earthquakes partly overlaps with the USGS one – especially for strong enough
 352 earthquakes – and so duplicates were removed when comparing these lists with the
 353 seismic activity recorded at EGO.

354 The control of the Virgo detector is extremely complex. Therefore, finding out how
 355 many earthquakes induced control losses during the O3 run required a careful study
 356 of all control losses, documented below in Appendix A. An earthquake from the list of
 357 USGS warnings is associated to a recorded control loss if the loss occurs within the time
 358 range during which seismic waves were predicted to arrive on-site according to Seismon
 359 and if the seismic activity around the time of the control loss is significantly larger
 360 than its typical range of variation. In case of concurring early warnings from different
 361 earthquakes overlapping by chance in time at EGO, the strongest is arbitrarily selected
 362 as the reason for the control loss.

363 Estimating the strength of an earthquake when its seismic waves arrive at EGO is not
 364 easy. Yet, this is a key point to address, first to reject quickly warnings from harmless
 365 earthquakes and then to adjust the latency and level of response for the crew in charge
 366 of steering the Virgo detector. During O3, basic rectangular cuts in the magnitude-
 367 distance plane – e.g. *if magnitude > (...) or (distance < (...) km and magnitude >*
 368 *(...)) or etc.* – were applied to the live earthquake warnings received from USGS and
 369 processed by Seismon. During the post-run analysis, the ranking

$$\text{ranking} = \frac{10^{\text{magnitude}/2}}{\text{distance}[\text{km}]} \quad (1)$$

370 was introduced. While not complete – e.g. neither the hypocenter depth nor its azimuth
 371 angle computed with respect to EGO are accounted for – this ranking appears sound:
 372 the higher its value, the more likely the control loss. And applying a minimum cut at
 373 0.02 on that ranking allows one to remove safely more than half of the earthquakes to
 374 be analyzed.

375 Results shown below use the largest possible earthquake statistics, meaning that the
 376 requirement on the Virgo status is that the detector is fully controlled, but not
 377 necessarily in Science mode. This looser requirement enlarges the dataset of interest
 378 and hence the number of earthquake early warnings to be taken into account.

379 Figure 10 highlights the epicenter distance and magnitude of the earthquakes that led
 380 to a Virgo control loss – called *delocks* in the captions. The top (bottom) row deals
 381 with the earthquake magnitude (epicenter distance) while the right column displays the

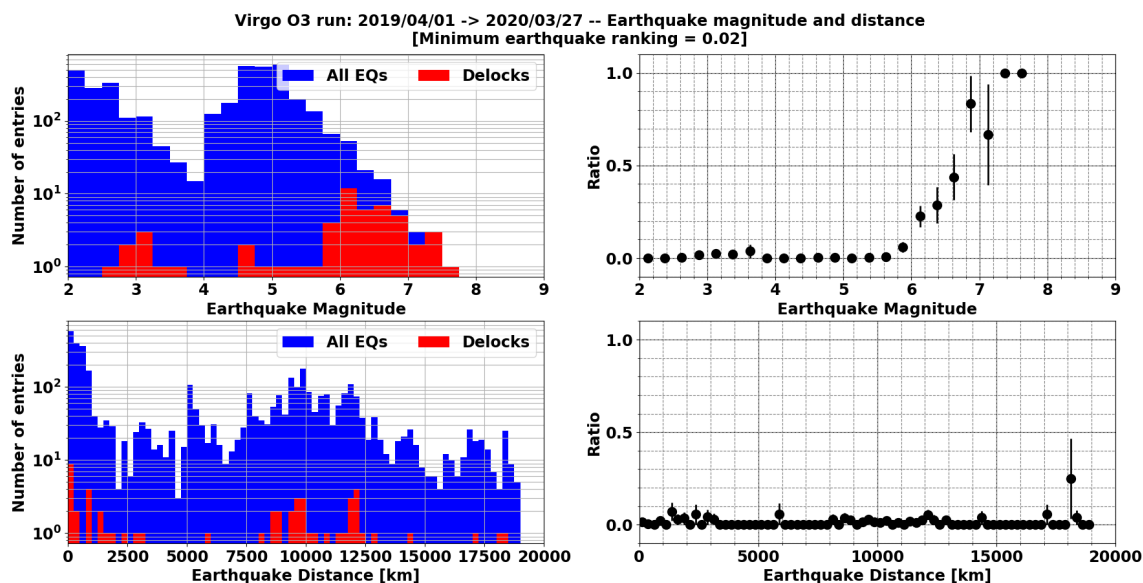


Figure 10: Summary of the impact of earthquakes on the Virgo detector during the O3 run. Left column: the blue (red) histogram shows all earthquakes (the earthquakes that have induced a control loss); top: magnitude distribution; bottom: distribution of the distance between EGO and the epicenter. Right column: corresponding fraction as a function of the earthquake magnitude (top) and distance (bottom). In all cases, the earthquakes that certainly could not impact Virgo (ranking below 0.02) were excluded.

382 ratio of the red and blue histograms shown on the left column. As expected, the larger
 383 the earthquake magnitude, the more likely the control loss: the fraction of earthquakes
 384 leading to a control loss takes off for magnitudes around 6, while magnitudes close to
 385 7 or above almost always cause a control loss. That ratio slightly departs from zero
 386 around a magnitude of 3: that small bump corresponds to the earthquakes close to
 387 Virgo and rather weak on the open Richter scale, but which are nevertheless strong
 388 enough to make Virgo lose its control. The same population of earthquakes is visible
 389 in the first bin of the epicenter distance histogram. The histogram ratio is much flatter
 390 for that other variable, with the most significant bins reflecting the location of seismic
 391 regions on the globe with respect to EGO, mainly the broad Mediterranean area and
 392 the Pacific Ring of Fire.

393 Figure 11 shows the population of earthquakes that caused a control loss (red dots) in
 394 the two-dimensional plane epicenter distance vs. magnitude. These earthquakes form
 395 the upper envelope of the scatter plot drawn, meaning they are usually the earthquakes
 396 with the largest magnitudes whose epicenter is located at a given distance from the
 397 EGO site. The separation between red and green (earthquakes that did not cause a
 398 control loss) dots is not perfect for at least two reasons. The first one is that the control
 399 of the Virgo detector is complex enough that the actual level of control (accuracy and
 400 stability) plays a role in whether or not the control is lost for earthquakes at the limits

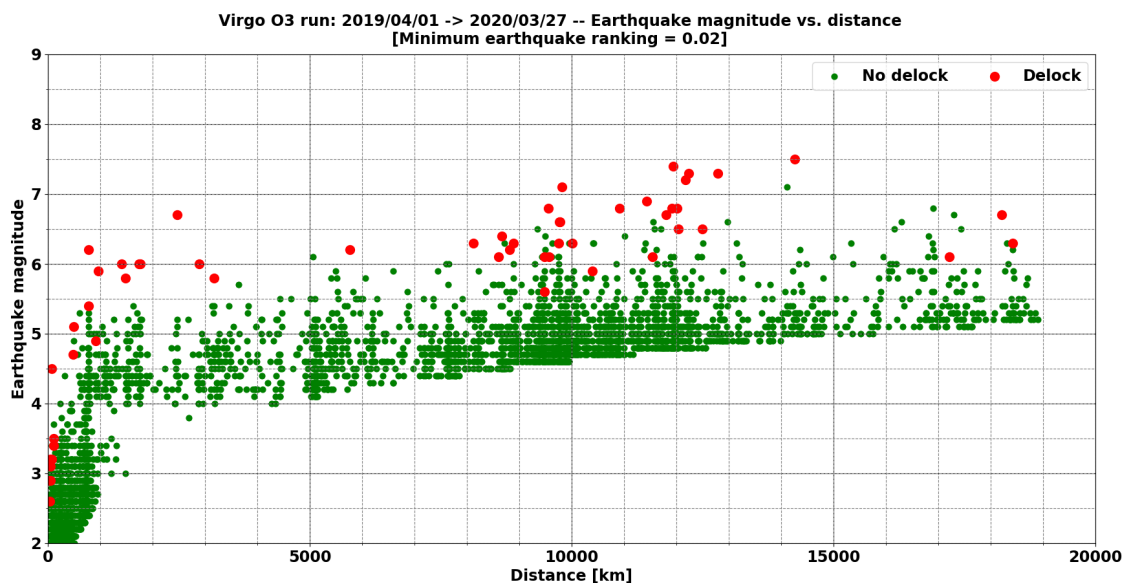


Figure 11: Distribution of earthquakes in the plane distance-magnitude during the O3 run. The earthquakes that caused a control loss (did not cause a control loss) are represented with red (green) dots. The lack of points below the main bulk of earthquakes is due to the ranking cut, set at 0.02.

401 of inducing a control loss. The second reason is that our model could probably be
 402 improved by including other earthquake warning parameters: two candidates would be
 403 the hypocenter depth (the deeper the hypocenter, the lower the earthquake impact on
 404 the ground at equivalent magnitude) and the azimuthal orientation of the epicenter with
 405 respect to EGO.

406 Figures 12 and 13 show the earthquake locations during the O3 run. Those associated
 407 with red dots have caused a control loss while those with a green marker have not. The
 408 boundaries of all major tectonic plates are clearly visible; as discussed above, the most
 409 harmful earthquakes for Virgo are coming from the Mediterranean area (medium to
 410 large magnitudes but smaller distances) and part of the Pacific Ring of Fire. The mid-
 411 Atlantic ridge and the Asian portion of the Alpidic earthquake belt did not produce many
 412 earthquakes that impacted Virgo, possibly because of the limited statistics. During the
 413 O3 run, the distribution of the earthquakes leading to control losses was the following:
 414 $\sim 15\%$ of close earthquakes; $\sim 20\%$ from other earthquakes in the Mediterranean area;
 415 and $\sim 65\%$ from distant earthquakes. This analysis will be updated in the future with
 416 data from the O4 run.

417 Finally, Fig. 14 shows an example of impact of a strong and distant earthquake on the
 418 Virgo detector and how using the early warning information to change the control mode
 419 prior to the arrival of the strongest seismic waves allowed to keep the working point of
 420 the instrument by preventing the correction force from saturating. Should that action
 421 not have been performed, the control loss would have been unavoidable. The description

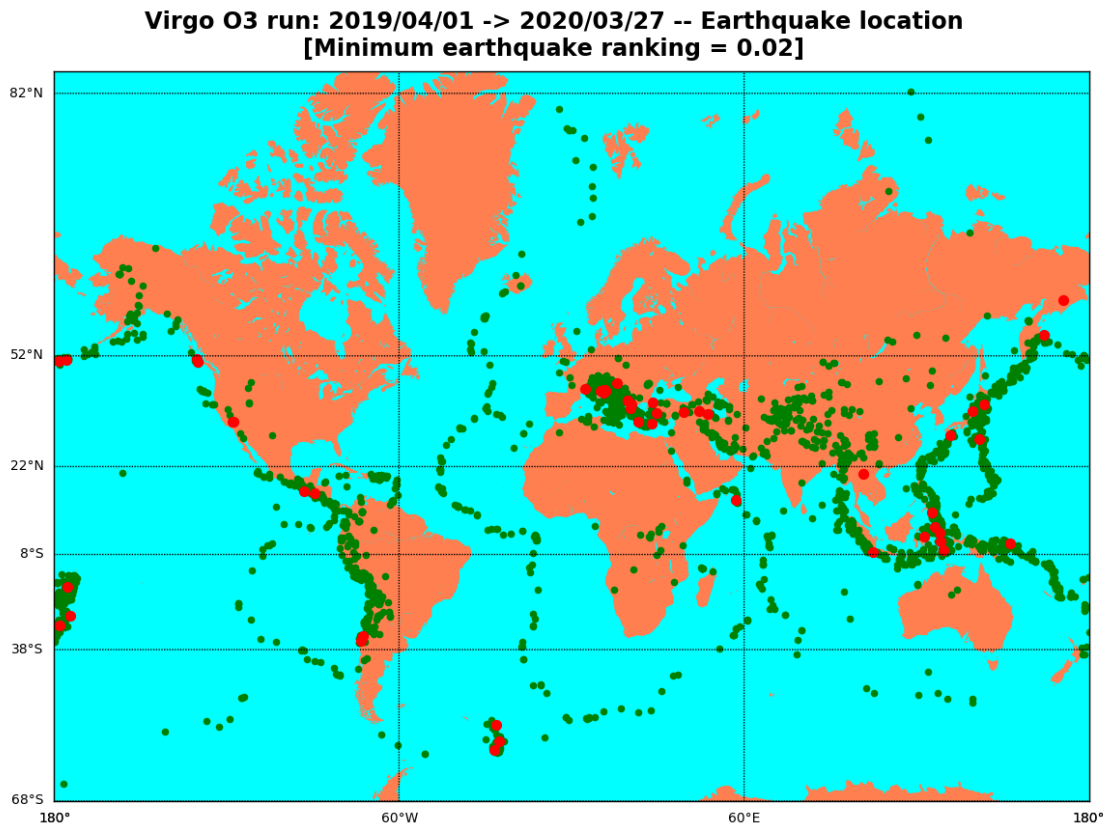


Figure 12: Earth location of the O3 earthquakes with ranking greater than 0.02. The earthquakes that caused a control loss (did not cause a control loss) are represented with red (green) dots.

422 of the different stripcharts displayed is given below.

- 423 ● Top plot: variation of the index labelling the Virgo data taking configuration – the
 424 Science mode – corresponds to the value 1; other indices shown here (-1, -7, -9)
 425 indicate other control configurations that are not nominal and that were used to
 426 wait for the right moment to switch back to Science data taking mode.
- 427 ● Second plot: stripchart of the BNS range versus time; the seismic waves clearly
 428 make the BNS range go down and fluctuate more while they are passing; the BNS
 429 range recovers its steady value at the end of the plotted time when the earthquake
 430 effect fades away.
- 431 ● Third plot: switch showing the times when the earthquake-resilient control mode
 432 ('EQ-mode') is turned on (0 → 1 transition) and later on off (1 → 0 transition)
 433 manually.
- 434 ● Fourth plot: For each second, maximum value of the correction applied on the test
 435 masses to keep the Virgo kilometric arms in resonance. When the nominal control
 436 mode is used, a control loss happens within two seconds at most after the time for

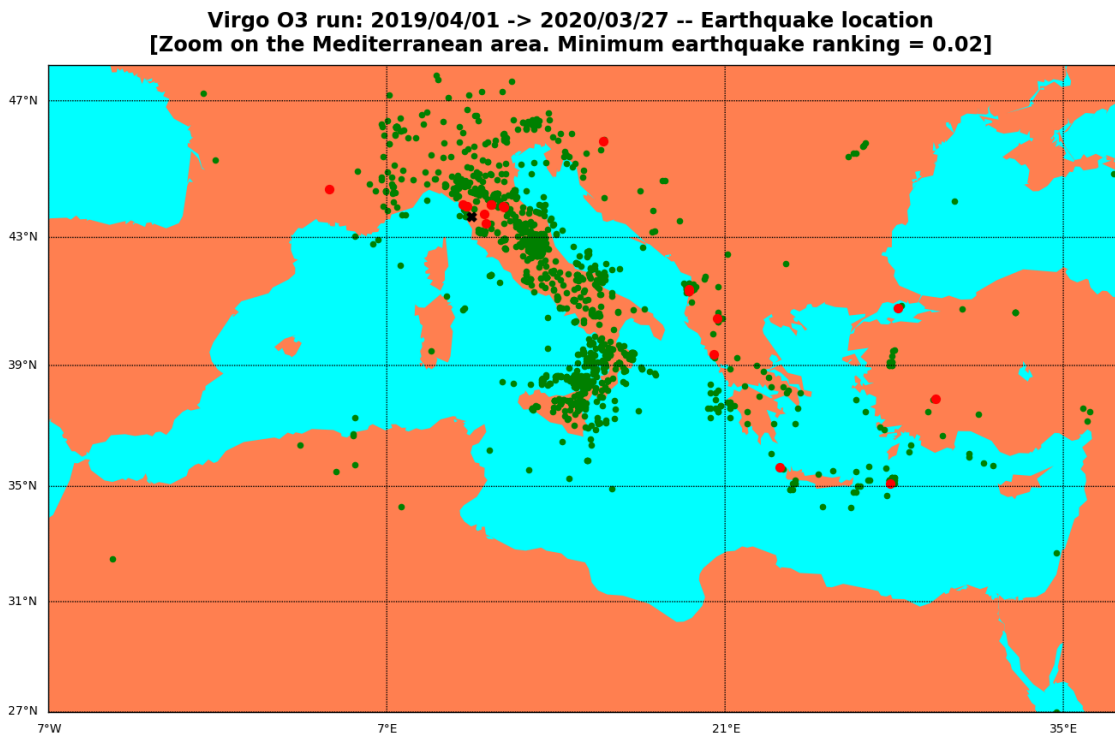


Figure 13: Zoom on the Mediterranean area of the map shown in Fig. 12 above. It shows the earthquakes nearby Virgo (whose site, EGO, is marked by a black cross) recorded during the O3 run. The earthquakes that caused a control loss (did not cause a control loss) are represented with red (green) dots.

437 which the correction exceeds a 9.5 V threshold. This occurs a few times close to
 438 the middle of the time range represented here but no control loss follows, as the
 439 EQ-mode allows for larger corrections.

- 440 ● Bottom plot: seismic noise measured in three orthogonal directions (vertical and
 441 along the two Virgo arms) using the telesism frequency range (10 mHz \rightarrow 100 mHz).
- 442 ● Finally, the vertical dashed lines common to all plots show the time of important
 443 events. From left to right: the time at which the earthquake occurred; the time
 444 at which the corresponding USGS warning had been received and processed by the
 445 Seismon framework; the expected arrival time of the seismic P- and S-waves; three
 446 different estimated arrival times for the seismic Rayleigh waves, depending on their
 447 speed (5, 3.5 and 2 km/s respectively).

448 4.3. Plans for O4

449 Work is in progress to build on the O3 experience and have a more performing, better
 450 integrated, earthquake early warning framework for O4 (and beyond). First, the plan

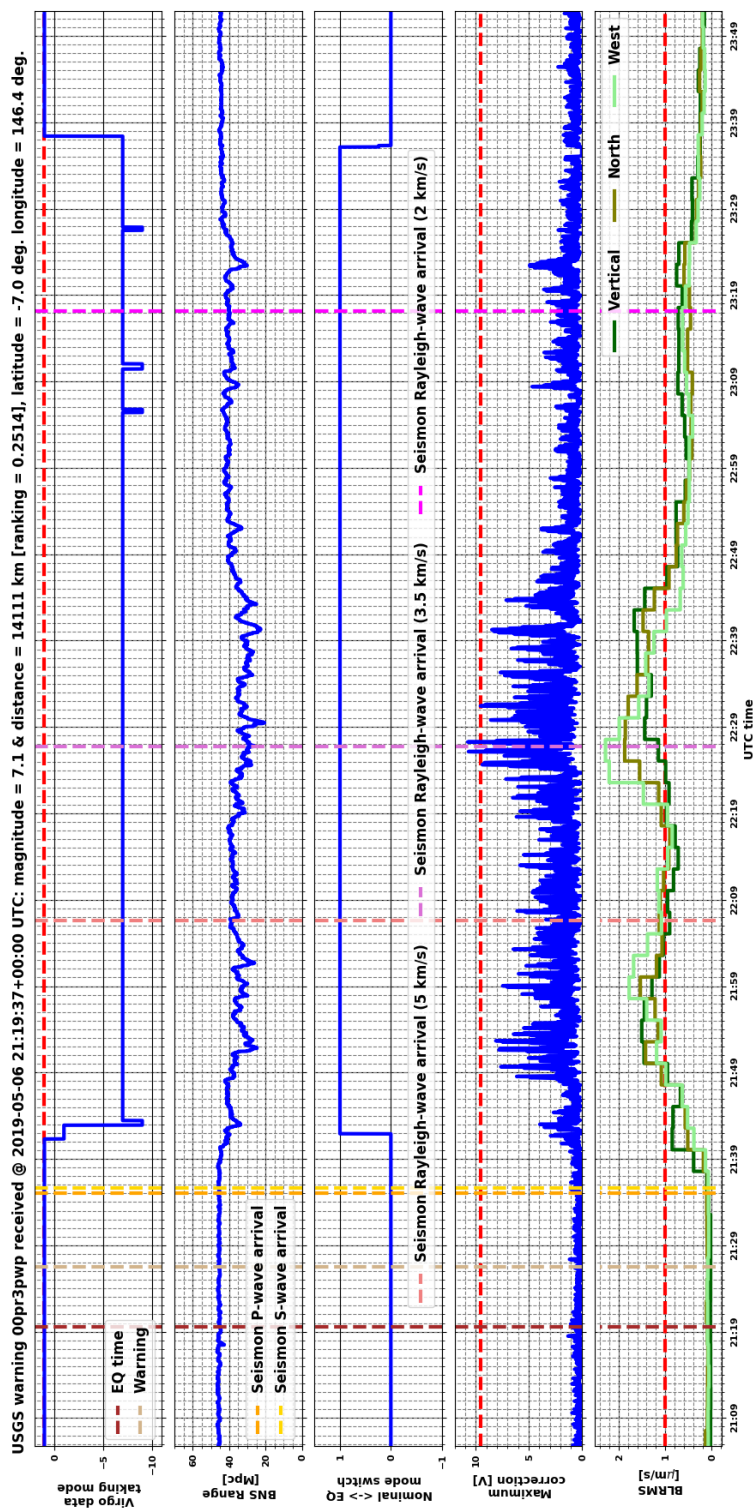


Figure 14: Example impact on the Virgo detector of a strong (magnitude greater than 7) and distant (14,000 km away from EGO) earthquake, that occurred on May 06, 2019. The description of the different stripcharts is provided in the text.

451 is to run the latest version of Seismon with an improved prediction capability for EGO,
 452 achieved by means of all the data collected during the O3 run. Then, we are exploring
 453 the possibility to use the INGV Early-Est system [35, 36] as an additional source of
 454 warnings, complementary to USGS. Tests are in progress to have this new live stream
 455 received at EGO and integrated into the existing framework. The two sets of early
 456 warnings will then be compared, in terms of latency and accuracy.

457 5. Bad weather

458 Through O3, the Virgo interferometer performed worst during days with adverse
 459 meteorological conditions, namely high winds and intense sea activity. These periods
 460 were generally associated with increased non-stationary noise in the GW signal below
 461 about 100 Hz and with some difficulty in maintaining the interferometer in the controlled
 462 state, resulting in reduced duty cycle. In the following, we study the impact of the
 463 increased microseismic noise associated to sea waves, then the influences of wind on BNS
 464 range, as well as the effect of wind gusts on the global interferometer controls. Because
 465 of the wind action on the sea surface, high winds and rough sea often occur together.
 466 We use a statistical approach to disentangle their effects on the detector.

467 5.1. Impact of sea activity

468 The intensity of microseism at the Virgo site increases by more than one order of
 469 magnitude between calm and rough sea periods. For 10% of the time during O3, ground
 470 RMS velocity between 0.1 Hz and 1 Hz was above 4 $\mu\text{m/s}$, as shown in Fig. 4. This
 471 happened in particular in correspondence of the seasonal change in the first part of O3b
 472 and for some periods of adverse weather condition in the first months of 2020. Periods
 473 of intense sea activity were associated to larger than usual strain residual noise whose
 474 characteristics and origin we investigated.

5.1.1. *Microseism impact on strain noise* Periods of high sea activity were associated
 with larger strain residual noise up to about 100 Hz. To characterize this effect, we
 made use of the *band-limited* RMS (BLRMS), defined for a generic signal, in a certain
 frequency band $[f_{\min}, f_{\max}]$, as:

$$\text{BLRMS}(t; [f_{\min}, f_{\max}]) := \sqrt{\int_{f_{\min}}^{f_{\max}} S(f; t) df}$$

475 where $S(f; t)$ is an estimate of the signal *power spectral density* (PSD) referred to a time
 476 t .

477 In Fig. 15, we report, for the entire O3 run, in blue the BLRMS of the strain in the
 478 band $[10, 20]$ Hz and, in red, the CEB seismometer BLRMS in the band $[0.1, 1]$ Hz. A

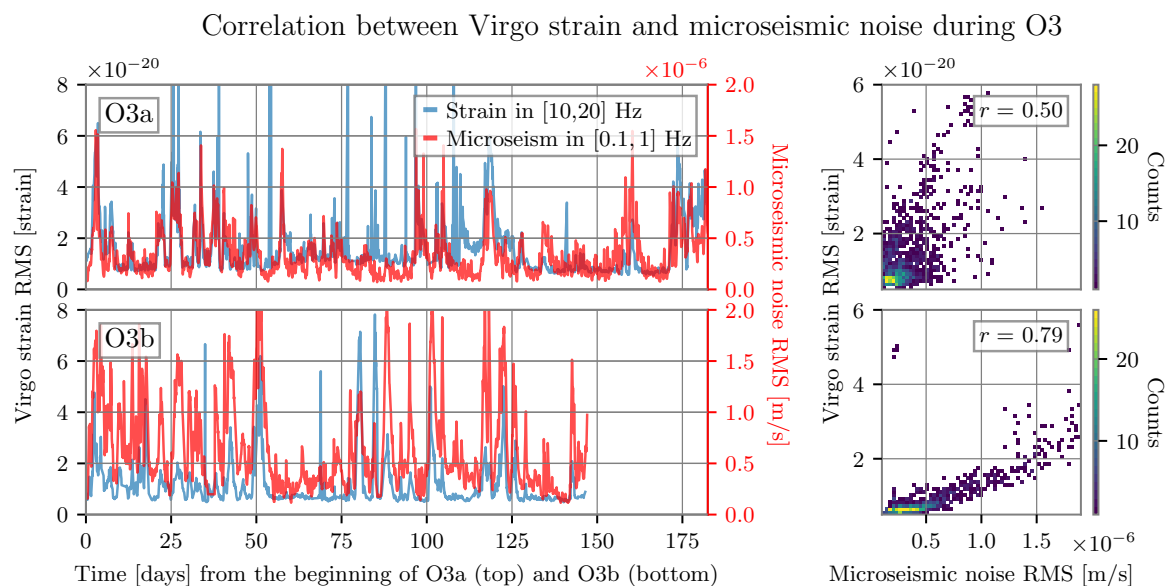


Figure 15: Correlation between the low frequency noise in Virgo GW strain and the microseism induced by the sea activity; top for O3a and bottom for O3b. Left: in blue the time series of the strain BLRMS in band $[10, 20]$ Hz and in red that of the BLRMS in band $[0.1, 1]$ Hz of a seismometer in the CEB, mostly influenced by the sea activity. Each value has been averaged over 2048 seconds of data. Right: 2D-histograms of the correlation between the two BLRMS, with the indication of their Pearson correlation coefficient r .

479 correlation between the two curves is evident. In particular, when the seismic BLRMS is
 480 large (intense microseism) the peaks in the former are almost everywhere coincident with
 481 those in the latter. This fact is also highlighted in the 2D-histograms on the right-hand
 482 side of the same figure, where the Pearson correlation coefficient has been computed for
 483 the two data taking periods, O3a (top) and O3b (bottom). In general, we observe that,
 484 despite the “spikes” in correspondence of bad weather conditions (in particular at the
 485 beginning of O3b and during most of Winter), the induced strain noise at low frequency
 486 has improved during O3.

487 *5.1.2. Microseism impact on glitch rates* Besides an increase in the RMS value of the
 488 strain noise at low frequency, microseism induces short transients of power excess in
 489 this signal, colloquially referred to as *glitches*. In Fig. 16 we report the minute rate of
 490 these glitches during the entire O3 run. To reduce the – usually very large – variability
 491 in their rate, we computed running daily medians. The gray dashed line represents the
 492 time evolution of daily medians for glitches with $\text{SNR} > 6.5$ and frequency at peak in
 493 the band $[10, 2048]$ Hz, as measured by the Omicron pipeline [37]. The blue solid line is
 494 the median minute rate of glitches with peak frequency in the $[10, 40]$ Hz band. These
 495 glitches accounted for about 30% of the total during O3a, and for almost 40% in O3b,

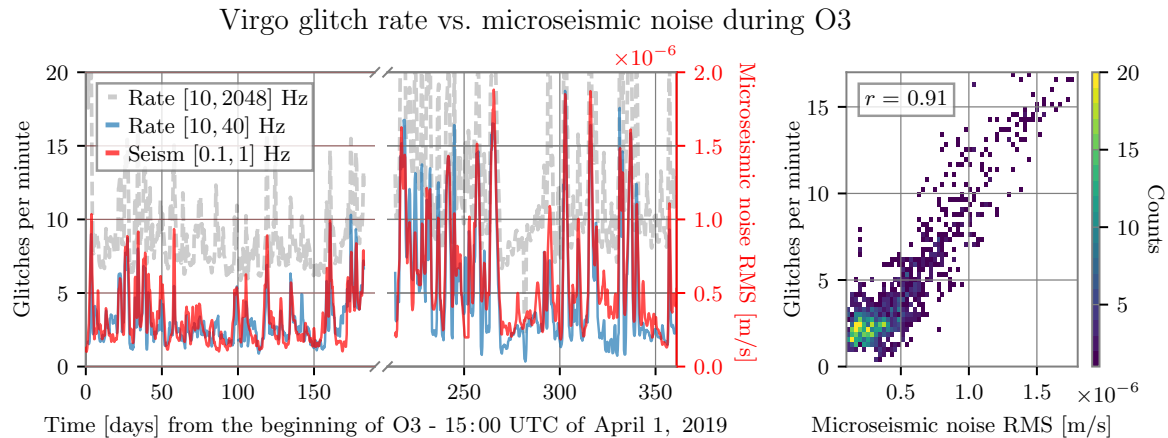


Figure 16: Correlation between Virgo glitch rate and the sea induced microseism during the O3 run. Left: the dashed gray line represents the daily moving median of the glitch rate per minute recorded by Omicron [37] for glitches with SNR > 6.5 and frequency at peak in band $[10, 2048]$ Hz, estimated over strides of 2048 seconds. The blue continuous line is the median rate referred to glitches with frequency at peak in $[10, 40]$ Hz band. The continuous red line is the BLRMS in band $[0.1, 1]$ Hz of a seismometer in the Virgo CEB. Right: 2D-histogram of the glitch rate in band $[10, 40]$ Hz and the microseism BLRMS, where also the value of their Pearson correlation coefficient r is reported.

496 with peaks larger than 80% in correspondence of periods of intense sea activity. This
 497 glitch rate is highly correlated with microseism due to sea activity, represented in the
 498 left-hand side plot of Fig. 16 by the solid red line of the running weekly median of the
 499 BLRMS in band $[0.1, 1]$ Hz of the CEB seismometer. On the right-hand side of the
 500 same figure, we report the 2D-histogram of these two quantities and the value of their
 501 Pearson coefficient ($r = 0.91$).

502 *5.1.3. Microseism and scattered light* Glitches due to microseism often resemble arches
 503 in a time-frequency map, as illustrated for example in Fig. 17. Arches are the typical
 504 signature of scattered light (SL) noise processes, which is a major issue and topic of
 505 investigation in the second generation GW detectors [11, 12, 13, 38, 39, 40].

506 A stray light beam bouncing off a moving surface adds constructively to the beam main
 507 mode every time its optical path, $x(t)$, changes (increases or decreases) by an integer
 508 wavelength. It follows that the frequency of the strain noise is:

$$f_{sc}(t) = \frac{2n|\dot{x}(t)|}{\lambda} \quad (2)$$

509 where $\dot{x}(t)$ is the instantaneous relative velocity between the interferometer beam and
 510 the scatterer, and $\lambda = 1.064 \mu\text{m}$ is the Virgo laser wavelength. Equation 2 is referred

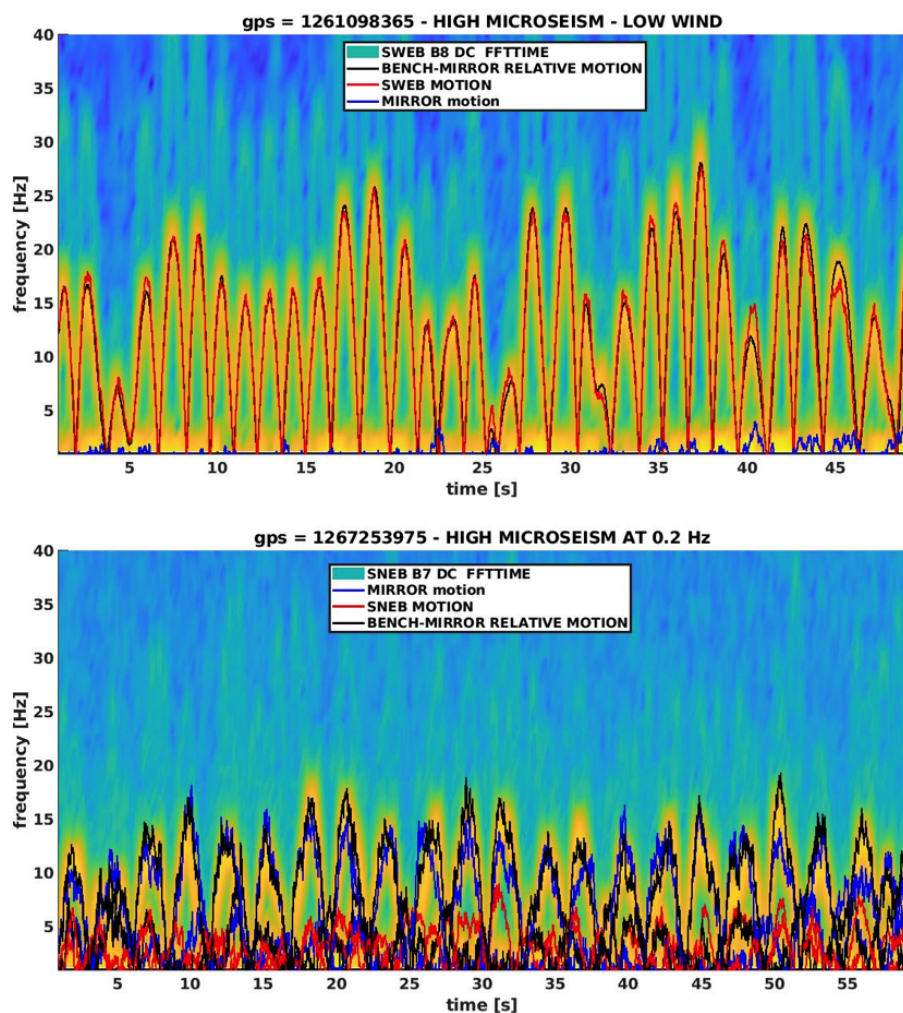


Figure 17: Spectrograms of the light transmitted at the end of the arm cavities and detected by photodiodes located behind, on suspended benches – top plot: west arm, B8 photodiode, SWEB bench; bottom plot: north arm, B7 photodiode, SNEB bench. The typical pattern of scattered light noise (arches) – both first order and second order (higher frequencies) – is visible. On the SWEB plot, arch spacing and amplitude correspond to half the period of marine microseism at Virgo (~ 3 s) and a ground velocity of about $8 \mu\text{m/s}$. The predictor for BENCH-MIRROR is shown in black, while the predictors computed from mirror and bench motions are shown in blue and red, respectively. The overlap shows that BENCH-MIRROR is the best predictor of scattered light, closely matching the observed arches.

511 to as predictor. In case the scattered beam encounters a second reflective surface it can
 512 bounce back and forth n times along the same path before recombining, giving rise to
 513 higher order noise arches, reaching out n -times larger frequencies.

514 In O3 the main sources of scattered light affecting the sensitivity were the suspended
 515 optical benches placed beyond the end test masses in the terminal buildings (SNEB,

516 SWEB). In this case, the noise observed in the time-frequency domain is well visible as
 517 power fluctuations in the cavity. The noise appears as a series of arches, where the typical
 518 non-stationarity and non-linearity of the noise is evident. Arch time spacing is the half-
 519 period of the oscillation of the mirror-bench relative motion, and arch amplitude (i.e.
 520 the maximum frequency extension of the induced strain noise) is $f_{max} = (4\pi/\lambda)AFn$
 521 where A and F are the amplitude and frequency of the oscillation. If the frequency
 522 and amplitude of the oscillation are such that $f_{max} > 10$ Hz, the noise affects the GW
 523 detection frequency band.

524 Being those benches suspended and controlled [41], their motion induced by the
 525 microseism was supposed to be attenuated enough to push the maximum frequency of
 526 the arches below 10 Hz. Moreover, a control technique taking into account the mirror-
 527 bench differential signals was implemented in order to reduce their relative motion
 528 (BENCH-MIRROR), which is the quantity effectively responsible of the noise coupling.

529 During O3, a malfunctioning was identified in the mechanical setting of the West
 530 Bench suspension (SWEB) which caused its actual motion to be comparable to the
 531 ground motion at the frequency of the main microseismic peak. Figure 17 shows the
 532 mirror contribution and the bench contribution to the arches separately, for both North
 533 and West cavity, in two selected bad-weather conditions. In the West arm power
 534 spectrogram, the typical pattern is visible: the arches were entirely due to SWEB
 535 motion, and all the times the ground motion exceeded a certain threshold during the
 536 run, these arches entered the detector band. In the North arm power spectrogram, the
 537 arches were normally much lower, and the contribution from the bench motion was of
 538 the same magnitude as the mirror motion. It was even possible to find some special
 539 conditions (the largest component of the ground motion centered at 0.2 Hz), in which
 540 the mirror motion was prevalent.

541 The issue concerning SWEB mechanics and control has been understood and cured after
 542 O3. In O4, its residual motion is expected to be at least similar to the one observed in
 543 O3 for SNEB. Further improvements in the control strategy will be tested for both the
 544 mirror and the bench suspension.

545 *5.1.4. Identification of scattered light culprits* Part of the effort regarding scattered
 546 light noise mitigation consists in the localisation of scattered light sources, referred
 547 to as culprit, through data analysis. This can be a difficult and time consuming
 548 operation in a km-long detector with many possible sources of SL. Adaptive algorithms
 549 for time series analysis can be used to this end, due to their ability to decompose
 550 nonlinear non-stationary data into a set of oscillatory modes [42, 43]. The methodology
 551 described in [43] and based on the time varying filter empirical mode decomposition (tvf-
 552 EMD) [44] adaptive algorithm is applied to the two data segments shown in Fig. 17.
 553 SL noise couples with the differential motion of the arm cavities (*DARM*, the Virgo
 554 longitudinal degree of freedom sensitive to GW) time series, which is first low-passed
 555 and then decomposed using tvf-EMD to extract its oscillatory modes, from which the

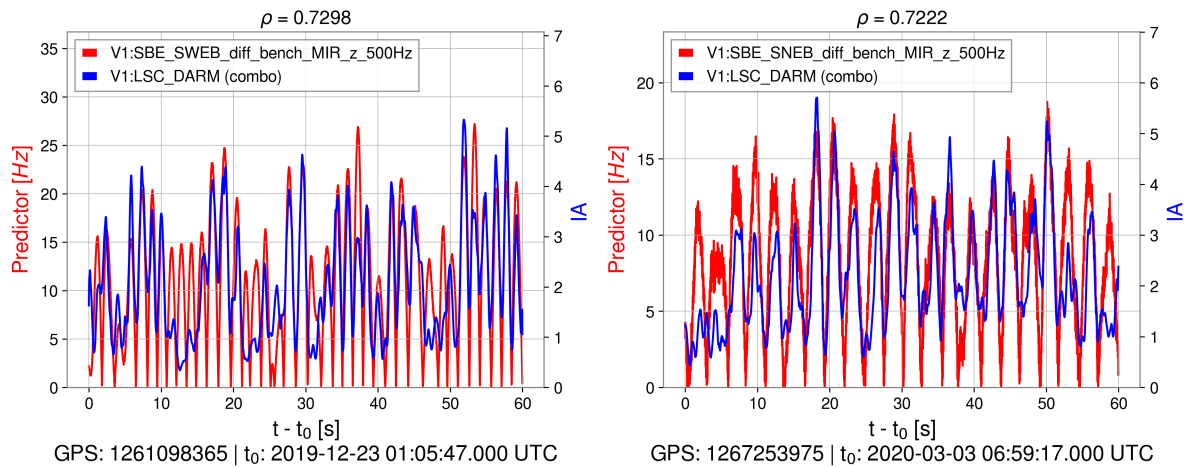


Figure 18: In red is the culprit’s predictor, i.e. Equation 2 for the relative motion (diff) between the suspended end bench and the end mirror (BENCH-MIRROR) of the West end (left) and North end (right). The sum of the IA of the first two modes of DARM, extracted by tvf-EMD is shown in blue.

556 instantaneous amplitude (IA) is obtained using the Hilbert transform. Computing
 557 Equation 2 for a broad list of position sensors and correlating with the IA of DARM’s
 558 oscillatory modes allows to quickly identify the most correlated channel, i.e. the culprit.
 559 The two data segment considered are

- 560 • GPS: 1261098365 UTC - 2019/12/23 01:05:47 + 60s,
- 561 • GPS: 1267253975 UTC - 2020/03/03 06:59:17 + 60s.

562 Obtained results are reported in Fig. 18, showing the predictors of the culprit for the end
 563 benches, based on Equation 2, correlated with the IA of DARM. The culprits are related
 564 to the BENCH-MIRROR channel in both cases. The resulting values of correlation are
 565 $\rho = 0.73$ for SWEB and $\rho = 0.72$ for SNEB. Since after low-passing the data the first
 566 two oscillatory modes of DARM were found to be the most correlated with the same
 567 predictor, the sum of their IA is considered and is shown in Fig. 18 for both cases,
 568 referred to as *combo*. As a counter proof, in Fig. 17 the predictors of the culprits are
 569 overlapped on the spectrograms of the WEB and NEB photodiodes. It can be seen
 570 that they closely match the scattered light arches. In particular, for the SWEB case,
 571 the mirror motion is small and the bench motion is mainly responsible for the observed
 572 scattered light. For SNEB case, while the mirror motion is significant the BENCH-
 573 MIRROR predictor, identified with adaptive analysis, better matches the arches also in
 574 this case.

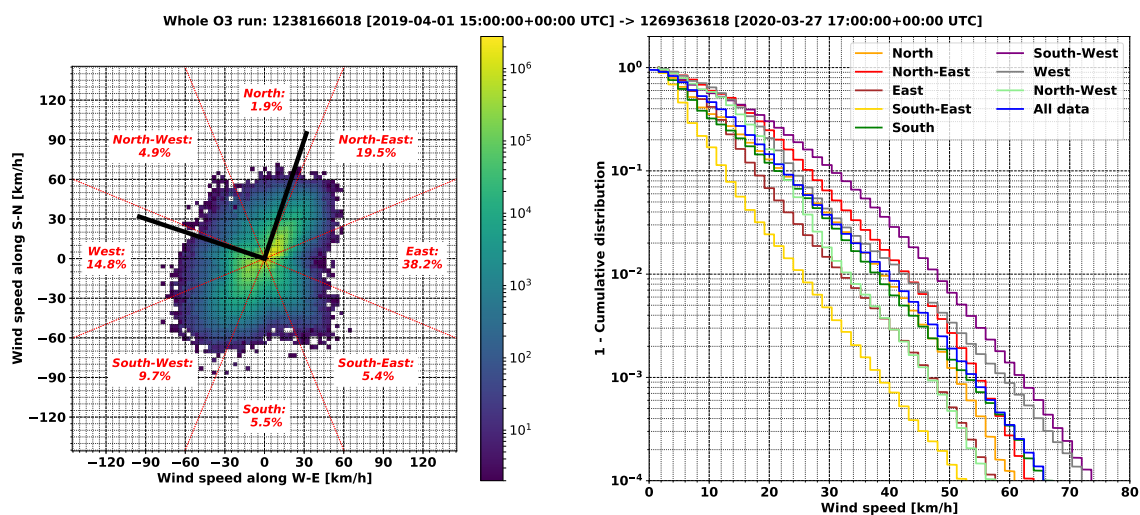


Figure 19: Wind statistics as measured by the EGO weather station during the O3 run. The left plot shows the distribution of the wind speed and orientation, with the two black bars showing the directions of the two arms of the Virgo detector. The right plot shows the complementary cumulative distribution of the wind speed for each of the eight quadrants of the wind rose.

575 5.2. Impact of wind

576 Figure 19 summarizes the wind statistics recorded at EGO during the O3 run. Wind is
 577 blowing more often from the East while the stronger winds are predominantly coming
 578 from the West – the sea shore.

579 The method described in Sec. 3.2.1 can be applied to quantify the impact of the
 580 instantaneous wind speed on the sensitivity. Figure 20 shows that the sensitivity is
 581 pretty much unaffected until a wind speed of $\sim 20 - 25$ km/h, while the detector gets
 582 sensitive to larger speeds: the BNS range decrease exceeds ~ 4 Mpc for a wind speed
 583 of 50 km/h or above. Yet this variation is limited (about 10% of nominal BNS range
 584 values during O3), meaning that the detector is quite robust against wind. Another
 585 consequence of high-wind conditions is the need for the Virgo global control system to
 586 use larger corrections to keep the instrument at its nominal working point. And the
 587 larger these corrections, the more the detector is vulnerable to additional disturbances
 588 that could make the corrections saturate and lead to an almost immediate control loss.

589 The effect of the wind speed is clearly visible on Fig. 21 that compares the
 590 complementary cumulative distribution functions of the kilometric Fabry-Perot cavity
 591 longitudinal corrections for different ranges of wind speed. Clearly, the larger the wind
 592 speed, the higher the correction. On this plot, the average wind speed and the maximum
 593 correction have been computed using non-overlapping time windows of 30 seconds each.
 594 The largest displayed correction range stops on purpose at 9 V because the actual
 595 physical correction saturates at 9.5 V, a value that can be reached or even exceeded

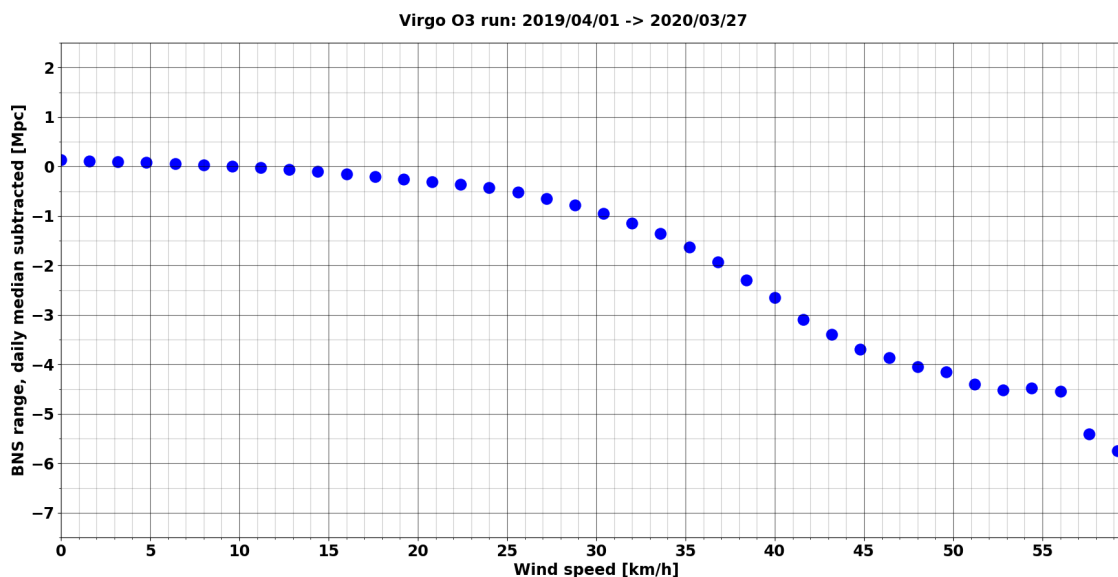


Figure 20: Average variation of the BNS range around its local average, as a function of the wind speed. In the Virgo DAQ, the BNS range and the wind speed are updated every 4 and 2 seconds, respectively.

596 when there is a control loss. As the control system has some small but non-zero internal
 597 latency, it is not always clear whether the observed saturation is the cause of the control
 598 loss or a consequence of it. Therefore, for a cumulative plot like the one shown on Fig. 21,
 599 corrections above 9 V have been cut away to avoid contamination from correction signals
 600 posterior to control losses.

601 5.3. Disentangling sea activity and wind

602 Bad weather conditions usually include both high microseism levels (due to the nearby
 603 rough sea) and high wind. Fig. 22 attempts to disentangle their impacts by looking at
 604 the O3 Virgo duty cycle as a function of the microseism level for three different wind
 605 conditions: no cut on wind speed (blue histogram); low wind speed (below 25 km/h,
 606 green); high wind speed (above 25 km/h, red). One can see that in low wind conditions
 607 the duty cycle is pretty much independent from microseismicity whereas it is lower and
 608 decreases more quickly when microseism levels increase. Therefore, the Virgo detector
 609 appears robust against microseism but more sensitive to wind. Note that the extreme
 610 bins on the histograms plotted on Fig. 22 may have low statistics compared to others
 611 (low wind and high microseism, or high wind and low microseism are rare conditions):
 612 this explains why the duty cycles reported there fluctuate significantly compared to
 613 neighboring bins.

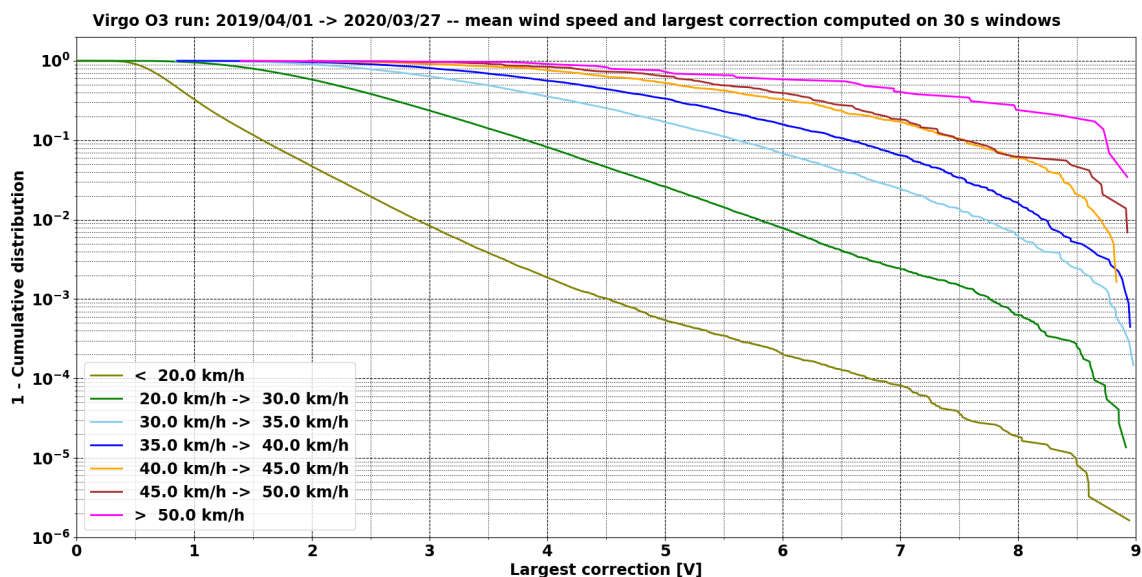


Figure 21: O3 complementary cumulative distribution functions of the maximum longitudinal corrections (in volts) keeping the Virgo arm cavities resonant for different wind speed ranges. The mean wind speed and the maximal corrections have been computed over 30 s time windows. The x -axis ends at 9 V, a bit below the saturation level of 9.5 V for that particular correction.

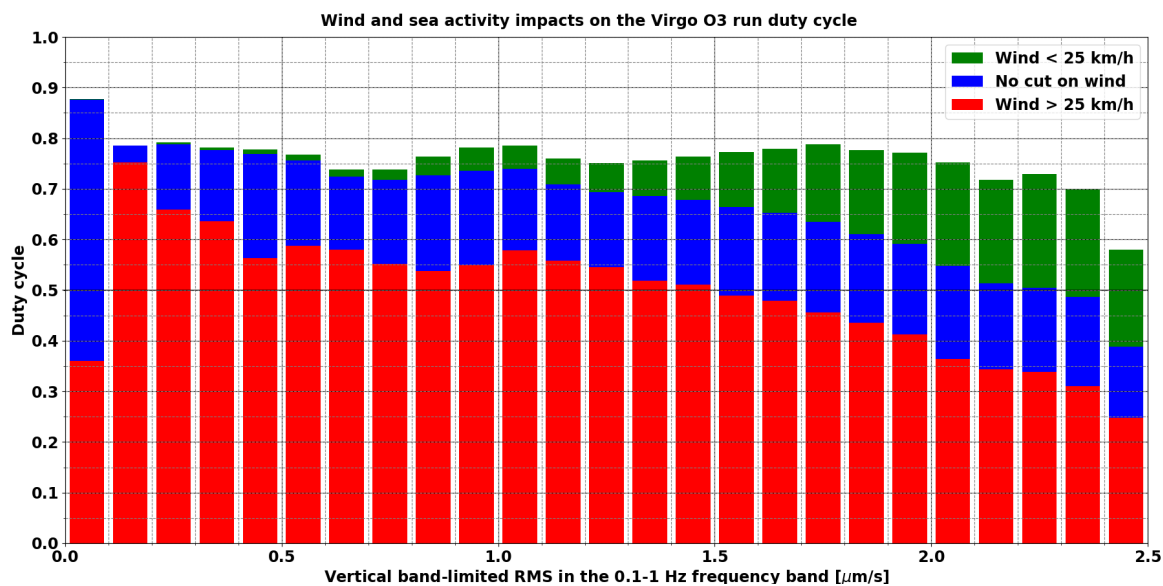


Figure 22: Virgo duty cycle during the O3 run versus microseism activity, for three different wind conditions: blue \leftrightarrow no cut on wind speed; green \leftrightarrow low wind (speed below 25 km/h); red \leftrightarrow high wind (speed above 25 km/h).

614 6. Other environment impacts

615 Additional sources of external noise have potential impact on the interferometer.
 616 Hereafter we describe those sources that we have further investigated during O3, namely:
 617 Schumann's magnetic fields, lightning strikes and cosmic ray muons.

618 6.1. Magnetic noise

619 Ambient magnetic fields can couple to GW interferometers, for example through the
 620 magnetic actuators used for the control of the seismic isolation platforms of optical
 621 components and of the test masses [11, 45]. Like gravitational waves, electromagnetic
 622 (EM) waves travel at the speed of light, and, due to their strength, could affect multiple
 623 detectors with the same timing as a GW. This is the case of Schumann magnetic field,
 624 large-current lightning strikes, and solar activity.

625 One purpose of the EGO external magnetometers (see Sec. 2) is to monitor the level of
 626 magnetic fields that extend over the entire planet and which can limit the sensitivity to
 627 GW signals correlated over multiple detectors [46, 47]. One such global field constitutes
 628 the Schumann's Resonances [48] (SR) consisting of steady EM waves that resonate inside
 629 the waveguide formed by the Earth surface and the ionosphere, and which are excited
 630 by globe-wide lightning activity.

631 At Virgo, the external magnetic environment is much quieter than inside experimental
 632 halls where stray magnetic fields are radiated by electric loads and cables circulating
 633 large currents. Figure 23 compares inside and outside magnetometer spectra recorded
 634 at Virgo during O3 and in the very quiet environment inside the Sos Enattos mine
 635 in Sardinia [49]. The most intense spectral noise are narrow lines at the 50 Hz electric
 636 mains frequency and its odd harmonics. The RMS amplitude of the 50 Hz line measured
 637 at Virgo is of the order of one tenth of a nT in the external location, while it is at least
 638 50 times larger in any inside location.

639 Virgo external magnetometers detect the Earth Schumann field. The second and third
 640 SR modes (peak frequency around 14 Hz and 21 Hz, respectively) are visible above
 641 noise at almost any time, their median amplitude during O3 is a few tenth of pT, their
 642 intensity follows a 24-hour modulation. The measured daily modulation of the third SR
 643 mode is shown in Fig. 24. This modulation is thought to be associated to temperature-
 644 driven variations in the height of the ionosphere EM waveguide [50]. The first SR mode
 645 and those of order greater than three, are often covered by anthropogenic magnetic
 646 noise. Figure 24 shows that during the COVID-19 lockdown period from March to May
 647 2020, the external magnetic field median RMS in the low frequency region from 1 to
 648 6 Hz reduced by about 50% with respect to the reference period between December
 649 2019 and February 2020. At the same time, the magnetic field RMS amplitude between
 650 18 Hz and 24 Hz around the 3rd Schumann mode, did not change appreciably.

651 At EGO, anthropogenic external magnetic noise follows a daily modulation: broad
 652 maxima during working hours and minima around 01:00 LT. The most intense
 653 disturbance comes in the form of short magnetic transients which we believe are
 654 associated to train transits along railway tracks at about 6 km distance from the
 655 site. The sudden trunk-line change when a train passes from an electro-duct section
 656 to another one creates stray currents and magnetic fields that are observed as magnetic
 657 glitches at the Virgo site. According to the measured coupling of ambient fields [11]
 658 we estimate a negligible impact of Schumann’s noise on the sensitivity of the future
 659 Virgo upgrades. More relevant might be the impact of the correlated Schumann noise
 660 on multiple interferometers, which is under evaluation.

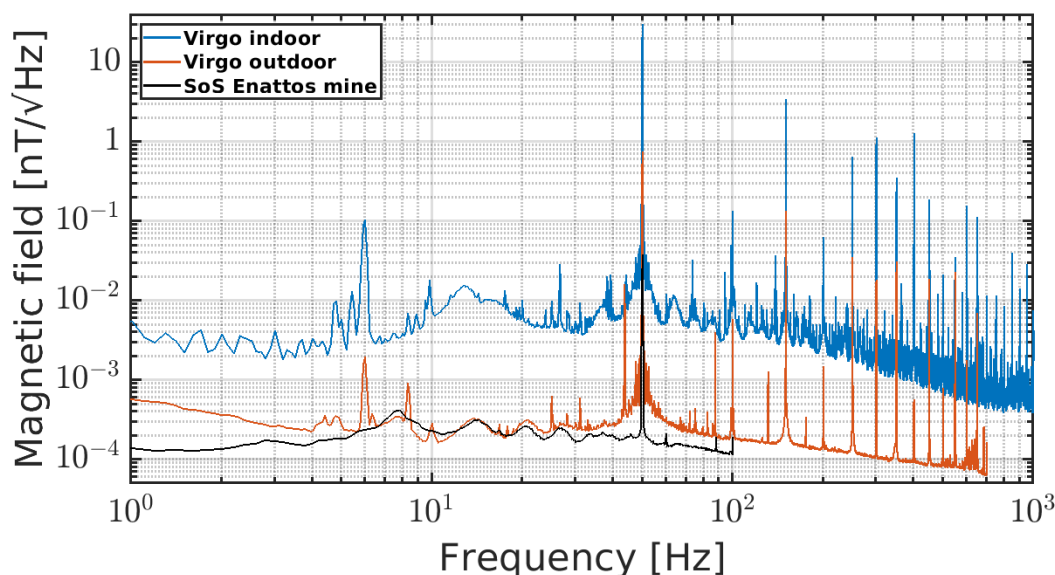


Figure 23: Amplitude spectral densities of indoor (blue curve) and outdoor (red curve) magnetometers at the Virgo site and at Sos Enattos mine in Sardinia (black curve). The quiet Sos Enattos location shows evidence of Schumann resonances peaked at approximately 8, 14, 21, 27 and 33 Hz.

661 6.2. Lightnings

662 Lightning strikes produce prompt EM waves and much slower air pressure waves which
 663 induce vibrations of the ground and of the detector mechanical components. There are
 664 studies of correlated lightnings noise between the Virgo and LIGO sites [47] and at the
 665 KAGRA underground observatory [51].

666 The typical effect of the impact of a lightning strike occurring at approximately 10
 667 kilometers from the Virgo detector during O3 is illustrated in Fig. 25. A distinctive
 668 feature of lightning strikes is a coincident short transient noise in magnetometers located
 669 inside the 3 km-distant Virgo experimental buildings (top graph of Fig. 25). The

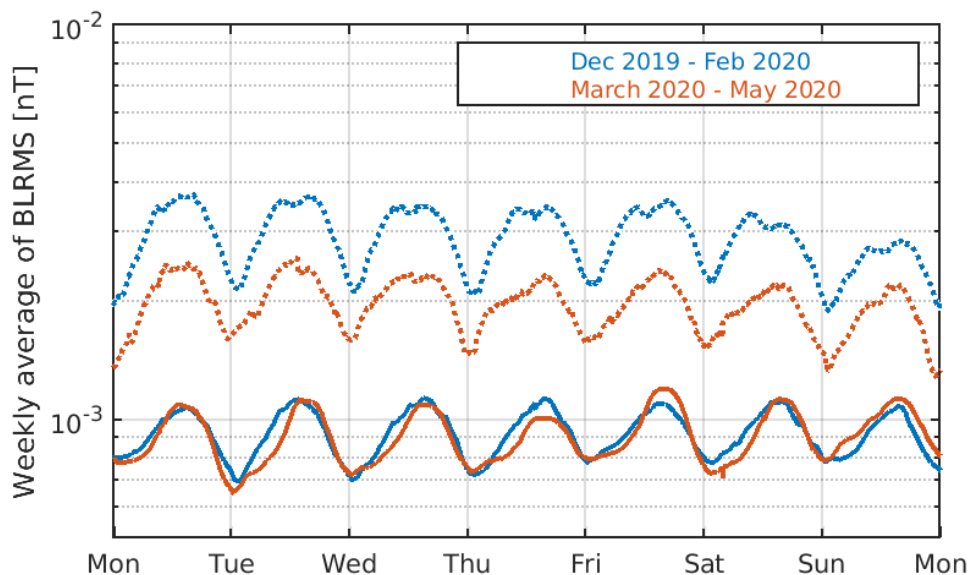


Figure 24: Weekly averaged magnetic field band-limited RMS value computed in two frequency bands: 1 to 6 Hz (dashed) and 18 to 24 Hz (solid). Magnetic field intensity is measured externally of Virgo experimental buildings, in the reference period between December 2019 and February 2020 (blue curves) and in the period between March 15 and May 15 (red curves) which corresponds to reduced anthropogenic activity within and outside of EGO because of the COVID-19 pandemic.

670 magnetic impulse is followed by the slower sound shock wave detected by seismometers
 671 (middle graph of Fig. 25). The bulk of displacement noise reaching the buildings is
 672 below 10 Hz.

673 The bottom graph of Fig. 25 illustrates the effect of the lightning in the GW strain signal.
 674 In coincidence with the spike in magnetometers, we observe a prompt broadband low-
 675 frequency noise and the onset of a 48 Hz narrow spectral noise, with a minute-long decay
 676 time, leading to a $\sim 30\%$ drop of the live BNS range. This latter noise has been associated
 677 to one structural mode of the West end test mass suspension, which gets excited because
 678 of the coupling of ambient magnetic fields with the magnetic actuators located along
 679 the suspension. Moreover, associated with the delayed acoustic and seismic bursts of
 680 ambient noise reaching the experimental buildings, a broadband strain noise shows up,
 681 extending up to about 100 Hz. This is likely due to scattered light processes within the
 682 interferometer.

683 Data quality flags active during lightning strikes were produced during the O3 run; they
 684 proved useful in a test aiming at filtering out part of the false-alarm triggers found by
 685 a real-time transient GW search [18]. Further studies are planned during the O4 run
 686 preparation.

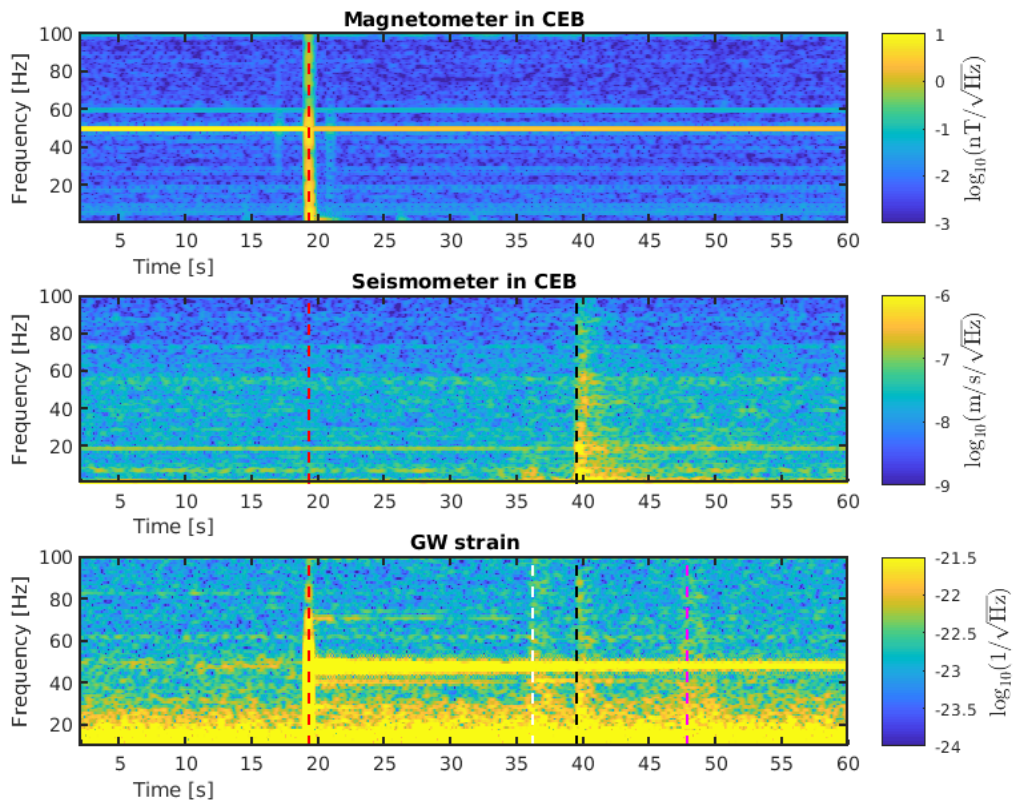


Figure 25: Impact on the Virgo environment and detector of one lightning strike which occurred 6 to 10 km away from Virgo buildings on November 15, 2019 at 23:25:51 UTC. The spectrograms of a few relevant signals are shown. (Top) A prompt magnetic transient is detected by magnetometers at the time of the event, marked by the red vertical line. (Middle) A few seconds later, a seismic (and acoustic, not shown) transient is detected in the central experimental area, marked by the black vertical line. The bottom spectrogram shows the GW strain reconstructed signal during the same time interval. The red vertical line marks the lightning strike occurrence, the black, magenta and white vertical lines mark the occurrence of seismic transients detected in the Central, North and West experimental buildings, respectively.

687 6.3. Cosmic muons

688 Ground-based GW detectors are constantly passed through by *muons*, produced by
 689 the interaction of cosmic rays with Earth's atmosphere [52]. This energetic charged
 690 particles can interact with the detector test masses and constitute an additional source
 691 of noise, as addressed in the literature since the first prototypes of resonant mass GW
 692 detectors [53, 54, 55, 56].

693 We report here the preliminary results on the first measurement of potential effects of
 694 these muons on the Virgo detector noise. Further result can be found in [57]. This study

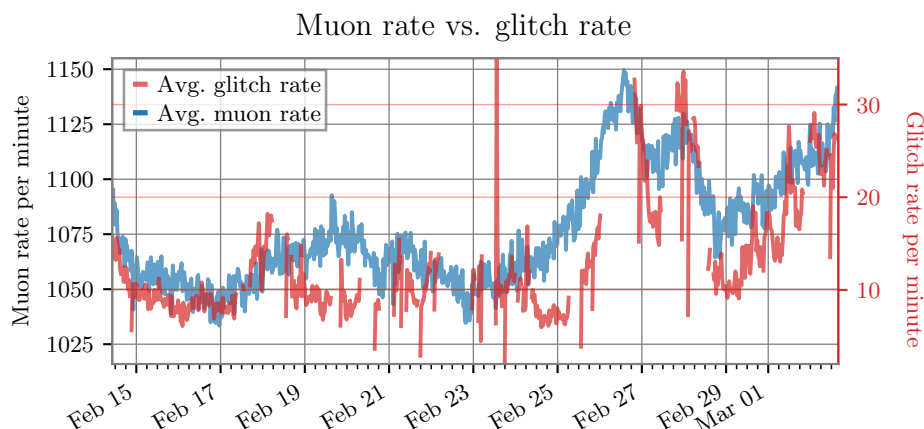


Figure 26: Correlation between muon and glitch rates. The blue line represents the time series of the average rate per minute of muons while the red one is the time series of the rate per minute of glitches with SNR > 4.5 and frequency at peak in $[10, 4096]$ Hz as identified by the Omicron pipeline [37]. Gaps in the latter correspond to periods when the detector was not in low noise conditions.

695 has been carried out by means of about 17 days, at the end of the O3b run, of joint data
 696 acquisition of Virgo and a muon telescope designed by the IP2I laboratory [58], installed
 697 in the CEB close to the beam splitter mirror. Two kind of tests have been performed.
 698 In the first one, we have evaluated whether the rate of muons in the correspondence of
 699 GW candidate events was larger than the reference values of the period: we have found
 700 no statistical evidence of an excess of muons in correspondence of these triggers. In the
 701 second test, we have estimated the correlation of this rate with the rate of glitches in
 702 Virgo noise. Figure 26 shows the time series corresponding to the rates of glitches and
 703 muons, averaged on strides of 30 minutes. Here, a correlation is clearly evident. This
 704 is actually not surprising, for the number of the muons arriving at ground being highly
 705 dependent on air density and ultimately on parameters like atmospheric pressure and
 706 temperature. These quantities are also witnesses of the weather conditions, which in
 707 turn can determine an increase of the detector noise, as we have commented in Sec. 5.1.
 708 Therefore, both the variations of these rates share the same main cause, which explain
 709 their large correlation. Once removed the effects of the atmospheric conditions via a
 710 regression analysis, the residuals exhibit no significant correlation.

711 7. Outlook and prospects for O4

712 The Virgo detector performances are affected by external environment conditions; in
 713 particular, seismic noise, earthquakes, bad weather, magnetic noise and lightnings have
 714 an impact on the detector sensitivity or duty cycle. The main coupling mechanisms are:
 715 direct excitation of suspended mirrors, vibration of experimental buildings, shaking of

716 benches hosting auxiliary optical systems, disturbances on critical electronic equipment.
717 If the detector control system is able to manage the effect of a disturbance, the
718 interferometer can remain locked with a reduced sensitivity, otherwise it unlocks and
719 the procedure to recover the working point has to be started again, thus impacting on
720 the duty cycle.

721 In this work we reported the results of the analysis of such events during the run O3.
722 Thanks to the large amount of data collected, we were able to perform a careful statistical
723 analysis of the impact of several kinds of external disturbances.

724 The results confirm that the Virgo detector is a very robust apparatus. The sensitivity
725 reduction due to anthropogenic seismic noise is very low: less than 2% in terms of BNS
726 range. Also the degradation due to the wind is limited: it appears only for wind speeds
727 larger than 25 km/h, reaching a sensitivity reduction as large as 10% only for very high
728 speed (larger than 50 km/h).

729 In these cases, the sensitivity reduction is due to an increased noise at low frequency as
730 well as to the appearance of short high frequency glitches. In few cases, such kind of
731 noise was indirectly originated by lightnings.

732 Both microseism and wind have an impact on the detector duty cycle, since the
733 increasing correction signals acting on the mirror during bad weather can saturate,
734 finally resulting to an unlock. It results that the Virgo detector global control is more
735 robust against microseism while it is less effective against strong wind.

736 The analysis of lock losses during O3 confirms that earthquakes are a relevant source
737 of unlock. The Seismon framework, useful to keep the detector in a safe state to avoid
738 unlocking during such events, was used during the whole O3 run and it is now being
739 upgraded for the next scientific run.

740 An upgrade of the environmental monitoring system is in progress to better face the
741 influence of external disturbances: installation of a new lightning detector in the central
742 area; installation of two additional weather stations at the end buildings to monitor local
743 wind gusts; and the installation of more sensitive accelerometers on locations prone to
744 light scattering (viewports, external optical benches, etc.).

745 These actions, together with several other upgrades of the Virgo detector, already
746 performed or presently in progress, will have a crucial role for the success of the next
747 scientific run O4, which is expected to start in the second half of 2022.

748 **Acknowledgements**

749 **October 2020 version** – <https://tds.virgo-gw.eu/q1/?c=15940>

750 The authors gratefully acknowledge the Italian Istituto Nazionale di Fisica Nucleare
751 (INFN), the French Centre National de la Recherche Scientifique (CNRS) and the

752 Netherlands Organization for Scientific Research, for the construction and operation
753 of the Virgo detector and the creation and support of the EGO consortium. The
754 authors also gratefully acknowledge research support from these agencies as well as by
755 the Spanish Agencia Estatal de Investigación, the Consellera d’Innovació, Universitats,
756 Ciència i Societat Digital de la Generalitat Valenciana and the CERCA Programme
757 Generalitat de Catalunya, Spain, the National Science Centre of Poland and the
758 Foundation for Polish Science (FNP), the European Commission, the Hungarian
759 Scientific Research Fund (OTKA), the French Lyon Institute of Origins (LIO),
760 the Belgian Fonds de la Recherche Scientifique (FRS-FNRS), Actions de Recherche
761 Concertées (ARC) and Fonds Wetenschappelijk Onderzoek – Vlaanderen (FWO),
762 Belgium. The authors gratefully acknowledge the support of the NSF, STFC, INFN,
763 CNRS and Nikhef for provision of computational resources.

764 *We would like to thank all of the essential workers who put their health at risk during*
765 *the COVID-19 pandemic, without whom we would not have been able to complete this*
766 *work.*

767 **Appendix A. Study of the lock losses during O3**

768 The Virgo detector needs to be controlled accurately in order to be sensitive to
769 gravitational-wave signals [16, 17]. Schematically, there is an automated procedure [18]
770 that brings the instrument from an initial state where the optics and the laser are
771 controlled independently one from another, to the nominal state where the different
772 optical cavities are jointly resonant and the interferometer itself is used as a length
773 etalon to control further the laser frequency. That procedure typically takes about
774 15-20 minutes and requires 1-2 attempts to complete. Then, the global control of the
775 detector is kept as long as possible, with feedback loops maintaining Virgo at its nominal
776 working point. When that control is lost for whatever reason, data taking stops and
777 the control acquisition procedure has to be started again. This leads to a decrease of
778 the instrument duty cycle and can cause transient gravitational waves to be missed.
779 Therefore, it is important to find out the causes of the control losses and to use this
780 information to improve the feedback systems and make them more robust.

781 As explained in Sec. 4 above, a global study of the control losses was needed to be
782 able to extract those likely due to earthquakes. It was decided to focus on the 601
783 control losses that occurred during O3 while the detector was taking data in nominal
784 conditions (Science mode), to be sure that no particular human action was happening
785 on the instrument at any of these times. Related to the duration of the O3 run (about
786 11 months) and to the duty cycle of the Virgo detector (about 75%), this corresponds
787 to about 1 control loss every 10 hours of data taking on average. And, in reality,
788 uninterrupted data taking stretches could be much longer as control losses usually cluster
789 in time when a particular problem impacts the detector.

ARM_POWER	DARK_FRINGE_SHUTTER	AUTOMATION_STATUS	Total
14	559	28	601

Table A1: Number of control losses witnessed first by each DAQ channel used to time accurately control losses. As expected, the two fast channels are by far those that detect a control loss first. Most of the time the fast shutter protecting the dark fringe photodiodes closes before the arm power loss gets large enough to trigger the other fast channel.

790 The first part of the study was to define the time the control loss occurred for each of
791 these events. For that we have used three different Virgo DAQ channels.

- 792 • Two fast channels, sampled at 10 kHz: `ARM_POWER`, latching when the power stored
793 in the kilometric arm cavities goes below some threshold, meaning that they are
794 not resonant anymore; `DARK_FRINGE_SHUTTER`, triggered when the fast shutter
795 protecting the dark fringe photodiodes from an excess of light [2] closes.
- 796 • One slow channel, sampled at 1 Hz: `AUTOMATION_STATUS`, monitoring the global
797 status of the detector, as seen by the automation process that steers the instrument.

798 The time of a control loss is defined as the earliest time one of these three switches flips
799 from its nominal value to the value corresponding to an uncontrolled detector. Most of
800 the time, as expected, the fast channels are the first ones to latch. And they do almost
801 simultaneously, given that the cavity resonance losses are all connected. Though, in
802 practice, the dark fringe shutter closes almost always before the cavity arm power has
803 decreased below its nominal threshold. In addition there are a few cases for which the
804 central automation system triggers first a shutdown of the detector global control, either
805 because it has detected an issue or because it has received a manual abort request from
806 the operator on duty. Table A1 shows the breakout of witnesses for the O3 control losses
807 that occurred while taking Science data.

808 Then, the selected strategy consists in testing several hypothesis in parallel for each
809 of these events – the main hypothesis investigated are listed in Tabs. A2 and A3 and
810 documented in the neighbouring text.

811 Various algorithms scanning the data around the control loss have thus been developed,
812 with the twofold goals of being

- 813 • *complete*: to have as many control losses as possible tagged by at least one control
814 loss hypothesis;
- 815 • *selective*: to find the right control loss origin as often as possible.

816 Achieving (close to) completeness requires testing many hypothesis, while a profusion
817 of algorithms could be detrimental to the selectivity of the method. Therefore, the

Error	Manual	Hardware	Control software	PI	Earthquakes	Total
2	10	92	7	2	30	143 (24%)

Table A2: Sure causes for 143 O3 control losses – see text for details.

818 classification starts with a subset of hypothesis, those that, when identified, certainly
 819 cause a control loss and are also very likely to be the root cause of that particular
 820 event. Obvious examples in that category – called *sure* in the following – are control
 821 losses induced manually by the operator on duty, or hardware problems unambiguously
 822 identified by the real-time monitoring system of the Virgo detector. These control
 823 loss hypothesis are independent by definition and the associated algorithms should be
 824 selective. This has been checked by processing the 601 O3 control losses studied. All
 825 these events have been associated with at most one control loss hypothesis belonging to
 826 the sure category: 24% with one, 76% with none.

827 Table A2 provides details about the 143 control losses whose cause has been tagged as
 828 sure, as described above. The dominant class is hardware problems, mainly transient
 829 interruptions of the data flow coming from some suspensions and causing feedback
 830 control systems to fail. The faulty components have been identified and replaced during
 831 the post-O3 shutdown and upgrade phase. Therefore, these problems are not expected
 832 to reoccur during the O4 run. Then, earthquakes are the second most common source
 833 of control losses in the sure category; about three times a month on average. Manual
 834 control losses induced by the operator on shift follow: they are due to the need to switch
 835 from nominal data taking to another task: weekly maintenance, regular calibration or
 836 commissioning activity. In O4 and beyond, such control losses should no longer occur as
 837 the procedure will be updated to require leaving Science mode before manually aborting
 838 the control. In 7 cases (only 1% of the total control losses) the source of the event could
 839 be traced to some software problem; 2 more cases were due to human errors.

840 Finally, two control losses are labelled as *PI* for parametric instabilities, an
 841 optomechanical phenomenon due to the interaction between optical and mechanical
 842 modes of the detector and that had been observed at LIGO in 2015 before finally
 843 being seen in Virgo as well in January 2020 [59]. If not mitigated, a PI can make
 844 control systems saturate in a deterministic way (meaning that the saturation will
 845 consistently reoccur as long as the detector remains in a configuration favourable for
 846 its appearance and growth), thus impacting the detector duty cycle. Moreover, it is
 847 impossible to predict exactly what combinations of the instrument parameters will lead
 848 to a PI. Therefore, a dedicated simulation framework has been developed to estimate
 849 the susceptibility of Virgo to PIs during O3, for O4, and beyond [60].

850 Table A3 describes how the remaining control losses ($\sim 76\%$) have been classified. 11%
 851 of the total remain unclassified, either because none of the hypothesis tested matched, or
 852 because too many did and there was no clear way to find out which one was the root cause

Fast unlocks	Actuation saturation	DARM control inaccuracy	Power loss in sidebands	Arm power asymmetry	Likely missing data	Automation decision	Others	Total
173	85	77	22	4	10	23	64 (11%)	458 (76%)

Table A3: Breakout of control losses by category. 64 (about 11% of the total number of control losses recorded in Science mode during the O3 Virgo run) control losses have not been accurately classified, either because none of the tested hypothesis seemed to match the recorded data or because too many hypothesis were found matching, making their classification inconclusive. Further studies will be done when pre-O4 control losses data become available, in order to make the current classification more complete.

853 (if identified). The largest category by far (29%) are the so-called *fast unlocks*, events
854 that are almost instantaneous and occur within the laser injection system, upstream of
855 the interferometer. Such control losses have been present for years, at rates that strongly
856 vary over time, ranging from crisis periods lasting some hours to very quiet times. Their
857 origin is not understood yet and dedicated studies are ongoing to understand the fast
858 unlock mechanism(s) and find ways to cure or at least mitigate that phenomenon. The
859 next five categories are all related to the variety of feedback control systems that are
860 running in parallel to keep the whole detector at its nominal working point. Improving
861 the accuracy and the robustness of these systems while making the instrument more
862 complex and thus more sensitive to the passing of gravitational wave is a permanent
863 challenge, taken up during each upgrade or commissioning phase.

864 The analysis of the O3 control losses has been made using two independent software
865 frameworks whose results have been compared: they have been found in good agreement,
866 in particular for the dominant control loss categories. With the experience gained during
867 O3, the goals for O4 are to improve the monitoring of the control losses and to reduce
868 the latency of their analysis. A software framework similar to the Data Quality Reports
869 (DQR) [18, 61, 62] used to vet in real time the gravitational-wave transient candidates
870 that are significant enough to trigger a public alert is under development. In this
871 analogy, the DQR signal candidates are replaced by the control losses and the set of
872 checks ran in parallel to assess the quality of the data around a candidate becomes
873 the various hypothesis that are tested for each control loss. This improved tool should
874 be available in the coming months, during the commissioning phase of the new double-
875 recycled Advanced Virgo detector and the associated noise hunting activities to improve
876 the overall sensitivity of the instrument.

877 References

- 878 [1] Aasi J *et al.* (LIGO Scientific) 2015 *Class. Quant. Grav.* **32** 074001 (*Preprint 1411.4547*)
879 [2] Acernese F *et al.* (Virgo Collaboration) 2015 *Class. Quant. Grav.* **32** 024001 (*Preprint 1408.3978*)

- 880 [3] Akutsu T *et al.* 2021 *Progress of Theoretical and Experimental Physics* **2021** ISSN 2050-
881 3911 05A102 (*Preprint* [https://academic.oup.com/ptep/article-pdf/2021/5/05A102/](https://academic.oup.com/ptep/article-pdf/2021/5/05A102/38109702/ptab018.pdf)
882 [38109702/ptab018.pdf](https://academic.oup.com/ptep/article-pdf/2021/5/05A102/38109702/ptab018.pdf)) URL <https://doi.org/10.1093/ptep/ptab018>
- 883 [4] Abbott B *et al.* (LIGO Scientific Collaboration, Virgo Collaboration) 2016 *Phys. Rev. Lett.* **116**
884 061102 (*Preprint* 1602.03837)
- 885 [5] Abbott B *et al.* (LIGO Scientific Collaboration, Virgo Collaboration) 2017 *Phys. Rev. Lett.* **119**
886 161101 (*Preprint* 1710.05832)
- 887 [6] Abbott B *et al.* (LIGO Scientific Collaboration, Virgo Collaboration, Fermi GBM, INTEGRAL,
888 IceCube Collaboration, AstroSat Cadmium Zinc Telluride Imager Team, IPN Collaboration,
889 Insight-HXMT Collaboration, ANTARES Collaboration, Swift Collaboration, AGILE Team,
890 1M2H Team, Dark Energy Camera GW-EM Collaboration, DES Collaboration, DLT40,
891 GRAWITA, Fermi-LAT Collaboration, ATCA, ASKAP, Las Cumbres Observatory Group,
892 OzGrav, DWF (Deeper Wider Faster Program), AST3 and CAASTRO Collaborations,
893 VINROUGE Collaboration, MASTER Collaboration, J-GEM, GROWTH, JAGWAR,
894 CaltechNRAO, TTU-NRAO and NuSTAR Collaborations, Pan-STARRS, MAXI Team,
895 TZAC Consortium, KU Collaboration, Nordic Optical Telescope, ePESSTO, GROND, Texas
896 Tech University, SALT Group, TOROS Collaboration, BOOTES Collaboration, MWA,
897 CALET Collaboration, IKI-GW Follow-up Collaboration, H.E.S.S. Collaboration, LOFAR
898 Collaboration, LWA, HAWC Collaboration, Pierre Auger Collaboration, ALMA Collaboration,
899 Euro VLBI Team, Pi of Sky Collaboration, Chandra Team at McGill University, DFN,
900 ATLAS Telescopes, High Time Resolution Universe Survey, RIMAS, RATIR, SKA South
901 Africa/MeerKAT) 2017 *Astrophys. J. Lett.* **848** L12 (*Preprint* 1710.05833)
- 902 [7] Abbott B *et al.* (LIGO Scientific Collaboration, Virgo Collaboration) 2019 *Phys. Rev. X* **9** 031040
903 (*Preprint* 1811.12907)
- 904 [8] Abbott R *et al.* (LIGO Scientific Collaboration, Virgo Collaboration) 2021 *Phys. Rev. X* **11** 021053
905 (*Preprint* 2010.14527)
- 906 [9] Abbott R *et al.* 2021 *The Astrophysical Journal Letters* **913** L7 URL [https://doi.org/10.3847/](https://doi.org/10.3847/2041-8213/abe949)
907 [2041-8213/abe949](https://doi.org/10.3847/2041-8213/abe949)
- 908 [10] Abbott R *et al.* (LIGO Scientific Collaboration and Virgo Collaboration) 2021 *Phys. Rev. D*
909 **103**(12) 122002 URL <https://link.aps.org/doi/10.1103/PhysRevD.103.122002>
- 910 [11] Fiori I *et al.* 2020 *Galaxies* **8** ISSN 2075-4434 URL <https://www.mdpi.com/2075-4434/8/4/82>
- 911 [12] Nguyen P *et al.* 2021 *Classical and Quantum Gravity* URL [http://iopscience.iop.org/](http://iopscience.iop.org/article/10.1088/1361-6382/ac011a)
912 [article/10.1088/1361-6382/ac011a](http://iopscience.iop.org/article/10.1088/1361-6382/ac011a)
- 913 [13] Washimi T *et al.* 2021 *Classical and Quantum Gravity* **38** 125005 URL [https://doi.org/10.](https://doi.org/10.1088/1361-6382/abf89a)
914 [1088/1361-6382/abf89a](https://doi.org/10.1088/1361-6382/abf89a)
- 915 [14] Punturo M *et al.* 2010 *Classical and Quantum Gravity* **27** 194002 URL [https://doi.org/10.](https://doi.org/10.1088/0264-9381/27/19/194002)
916 [1088/0264-9381/27/19/194002](https://doi.org/10.1088/0264-9381/27/19/194002)
- 917 [15] Acernese F *et al.* 2004 *Astroparticle Physics* **20** 629–640 ISSN 0927-6505 URL [https://www.](https://www.sciencedirect.com/science/article/pii/S0927650503002603)
918 [sciencedirect.com/science/article/pii/S0927650503002603](https://www.sciencedirect.com/science/article/pii/S0927650503002603)
- 919 [16] Acernese F *et al.* 2020 *Astroparticle Physics* **116** 102386 ISSN 0927-6505 URL [https://www.](https://www.sciencedirect.com/science/article/pii/S0927650519301835)
920 [sciencedirect.com/science/article/pii/S0927650519301835](https://www.sciencedirect.com/science/article/pii/S0927650519301835)
- 921 [17] Allocca A *et al.* 2020 *Galaxies* **8** ISSN 2075-4434 URL <https://www.mdpi.com/2075-4434/8/4/85>
- 922 [18] The Virgo Collaboration 2021 *In preparation*
- 923 [19] Barone F, De Rosa R, Eleuteri A, Milano L and Qipiani K 2002 *IEEE Transactions on Nuclear*
924 *Science* **49** 405–410
- 925 [20] RADIO WAVES below 22 kHz URL <http://www.vlf.it/>
- 926 [21] Koley S *et al.* 2017 *SEG Technical Program Expanded Abstracts* 2946–2950 URL [https://doi.](https://doi.org/10.1190/segam2017-17681951.1)
927 [org/10.1190/segam2017-17681951.1](https://doi.org/10.1190/segam2017-17681951.1)
- 928 [22] Longuet-Higgins M S 1950 *Philosophical Transactions of the Royal Society of London. Series A,*
929 *Mathematical and Physical Sciences* **243** 1–35
- 930 [23] Cessaro R K 1994 *Bulletin of the Seismological Society of America* **84** 142–148

- 931 [24] Peterson J R 1993 *Open-File Report* URL <http://pubs.er.usgs.gov/publication/ofr93322>
- 932 [25] Flamini R 2020 Status and plans of the Virgo gravitational wave detector *Ground-based and*
933 *Airborne Telescopes VIII* vol 11445 ed Marshall H K, Spyromilio J and Usuda T International
934 Society for Optics and Photonics (SPIE) pp 205 – 214 URL [https://doi.org/10.1117/12.](https://doi.org/10.1117/12.2565418)
935 2565418
- 936 [26] Coughlin M *et al.* 2017 *Classical and Quantum Gravity* **34** 044004 URL [https://doi.org/10.](https://doi.org/10.1088/1361-6382/aa5a60)
937 1088/1361-6382/aa5a60
- 938 [27] Biscans S *et al.* 2018 *Classical and Quantum Gravity* **35** 055004 URL [https://doi.org/10.1088/](https://doi.org/10.1088/1361-6382/aaa4aa)
939 1361-6382/aaa4aa
- 940 [28] Mukund N *et al.* 2019 *Classical and Quantum Gravity* **36** 085005 URL [https://doi.org/10.](https://doi.org/10.1088/1361-6382/ab0d2c)
941 1088/1361-6382/ab0d2c
- 942 [29] Product distribution layer git repository URL <https://github.com/usgs/pdl>
- 943 [30] Berni F *et al.* 2012 The Detector Monitoring System <https://tds.virgo-gw.eu/ql/?c=9005>
- 944 [31] F Berni 2020 DMS help manual <https://tds.virgo-gw.eu/ql/?c=15469>
- 945 [32] 2020 Virgo logbook entry validating the use of the eq mode control configuration to take science-
946 quality data URL <https://logbook.virgo-gw.eu/virgo/?r=48612>
- 947 [33] 2020 Query to the public ingv website URL [http://webservices.ingv.it/fdsnws/event/](http://webservices.ingv.it/fdsnws/event/1/query?starttime=2019-04-01T15%3A00%3A00&endtime=2020-03-27T17%3A00%3A00&minmag=2&maxmag=10&mindepth=-10&maxdepth=1000&minlat=27.0&maxlat=48.0&minlon=-7.0&maxlon=37.5&mininversion=100&orderby=time-asc&timezone=UTC&format=text&limit=10000)
948 1/query?starttime=2019-04-01T15%3A00%3A00&endtime=2020-03-27T17%3A00%3A00&
949 minmag=2&maxmag=10&mindepth=-10&maxdepth=1000&minlat=27.0&maxlat=48.0&minlon=
950 -7.0&maxlon=37.5&mininversion=100&orderby=time-asc&timezone=UTC&format=text&
951 limit=10000
- 952 [34] INGV seismic surveillance center public website URL <http://terremoti.ingv.it>
- 953 [35] Bernardi F *et al.* 2015 *Natural Hazards and Earth System Sciences* **15** 2019–2036 URL [https://](https://nhess.copernicus.org/articles/15/2019/2015/)
954 nhess.copernicus.org/articles/15/2019/2015/
- 955 [36] Early-est: Earthquake rapid location system with estimation of tsunamigenesis URL [http://](http://early-est.rm.ingv.it/warning.html)
956 early-est.rm.ingv.it/warning.html
- 957 [37] Robinet F *et al.* 2020 *SoftwareX* **12** 100620 ISSN 2352-7110 URL [https://www.sciencedirect.](https://www.sciencedirect.com/science/article/pii/S2352711020303332)
958 [com/science/article/pii/S2352711020303332](https://www.sciencedirect.com/science/article/pii/S2352711020303332)
- 959 [38] Canuel B, Genin E, Vajente G and Marque J 2013 *Opt. Express* **21** 10546–10562 URL [http://](http://www.opticsexpress.org/abstract.cfm?URI=oe-21-9-10546)
960 www.opticsexpress.org/abstract.cfm?URI=oe-21-9-10546
- 961 [39] Waş M, Gouaty R and Bonnard R 2021 *Classical and Quantum Gravity* **38** 075020 URL
962 <https://doi.org/10.1088/1361-6382/abe759>
- 963 [40] Accadia T *et al.* 2010 *Classical and Quantum Gravity* **27** 194011 URL [https://doi.org/10.](https://doi.org/10.1088/0264-9381/27/19/194011)
964 1088/0264-9381/27/19/194011
- 965 [41] Van Heijningen J V *et al.* 2019 *Class. Quant. Grav.* **36** 7 URL [https://iopscience.iop.org/](https://iopscience.iop.org/article/10.1088/1361-6382/ab075e)
966 [article/10.1088/1361-6382/ab075e](https://iopscience.iop.org/article/10.1088/1361-6382/ab075e)
- 967 [42] Valdes G, O’Reilly B and Diaz M 2017 *Class. Quant. Grav.* **34** 235009
- 968 [43] Longo A *et al.* 2020 *Class. Quant. Grav.* **37** 145011 (*Preprint* 2002.10529)
- 969 [44] Li H, Li Z and Mo W 2017 *Signal Processing* **138**
- 970 [45] Cirone A *et al.* 2018 *Rev. Sci.* **89** 114501 URL <https://doi.org/10.1063/1.5045397>
- 971 [46] Coughlin M W *et al.* 2018 *Phys. Rev. D* **97**(10) 102007 URL [https://journals.aps.org/prd/](https://journals.aps.org/prd/abstract/10.1103/PhysRevD.97.102007)
972 [abstract/10.1103/PhysRevD.97.102007](https://journals.aps.org/prd/abstract/10.1103/PhysRevD.97.102007)
- 973 [47] Kowalska-Leszczynska I *et al.* 2017 *Classical and Quantum Gravity* **34** 074002 URL [https://](https://doi.org/10.1088/1361-6382/2Faa60eb)
974 doi.org/10.1088/1361-6382/2Faa60eb
- 975 [48] Schumann W 1952 *Zeitschrift Naturforschung Teil A* **7** 149
- 976 [49] Naticchioni L *et al.* 2020 *Journal of Physics: Conference Series* **1468** 012242 URL [https://](https://doi.org/10.1088/1742-6596/1468/1/012242)
977 doi.org/10.1088/1742-6596/1468/1/012242
- 978 [50] Sentman, D D 1995 *Schumann Resonances* (CRC Press) chap 11
- 979 [51] Washimi T *et al.* 2021 *Journal of Instrumentation* **16** P07033 URL [https://doi.org/10.1088/](https://doi.org/10.1088/1748-0221/16/07/p07033)
980 1748-0221/16/07/p07033
- 981 [52] Maurin D, Melot F and Taillet R 2014 *Astronomy & Astrophysics* **569** A32

- 982 [53] Beron B L and Hofstadter R 1969 *Phys. Rev. Lett.* **23**(4) 184–186 URL [https://link.aps.org/](https://link.aps.org/doi/10.1103/PhysRevLett.23.184)
983 [doi/10.1103/PhysRevLett.23.184](https://link.aps.org/doi/10.1103/PhysRevLett.23.184)
- 984 [54] Amaldi E and Pizzella G 1986 *Il Nuovo Cimento C* **9** 612–620
- 985 [55] Giazotto A 1988 *Physics Letters A* **128** 241–244 ISSN 0375-9601
- 986 [56] Chiang J, Michelson P and Price J 1992 *Nuclear Instruments and Methods in Physics Research*
987 *Section A: Accelerators, Spectrometers, Detectors and Associated Equipment* **311** 603–612 ISSN
988 0168-9002
- 989 [57] The ENV team 2021 Future publication about muons separate paper about Virgo and cosmic
990 muons
- 991 [58] Lesparre N *et al.* 2012 *Geoscientific Instrumentation, Methods and Data Systems* **1** 33–42 URL
992 <https://gi.copernicus.org/articles/1/33/2012/>
- 993 [59] Puppo, P for the Virgo Collaboration 2021 Parametric Instability Observation in Advanced
994 Virgo second European Physical Society Conference on Gravitation: measuring gravity
995 URL [https://agenda.infn.it/event/26098/contributions/132480/attachments/83185/](https://agenda.infn.it/event/26098/contributions/132480/attachments/83185/109525/EPS_Online2021_PI.pdf)
996 [109525/EPS_Online2021_PI.pdf](https://agenda.infn.it/event/26098/contributions/132480/attachments/83185/109525/EPS_Online2021_PI.pdf)
- 997 [60] Cohen D *et al.* 2021 Towards optomechanical parametric instabilities prediction in ground-based
998 gravitational wave detectors (*Preprint* 2102.11070)
- 999 [61] The LIGO Scientific Collaboration and The Virgo Collaboration 2018 Data Quality Report User
1000 Documentation <https://docs.ligo.org/detchar/data-quality-report>
- 1001 [62] Davis D *et al.* 2021 *Classical and Quantum Gravity* **38** 135014 URL [https://doi.org/10.1088/](https://doi.org/10.1088/1361-6382/abfd85)
1002 [1361-6382/abfd85](https://doi.org/10.1088/1361-6382/abfd85)